A MULTISCALE VISION — ILLUSTRATIVE APPLICATIONS FROM BIOLOGY TO ENGINEERING

Tamar Schlick,[1,2,3,*] Stephanie Portillo-Ledesma,[1] Mischa Blaszczyk,[4] Luke Dalessandro,[5] Somnath Ghosh,[6] Klaus Hackl,[7] Cale Harnish,[8] Shravan Kotha,[6] Daniel Livescu,[9] Arif Masud,[10] Karel Matouš,[11] Arturo Moyeda,[12] Caglar Oskay,[13] & Jacob Fish[14]

[1]*Department of Chemistry, New York University, New York, New York 10003, USA*
[2]*Courant Institute of Mathematical Sciences, New York University, New York, New York 10012, USA*
[3]*NYU-ECNU Center for Computational Chemistry, NYU Shanghai, China*
[4]*Institute of Mechanics of Materials, Ruhr-University Bochum, Bochum 44721, Germany*
[5]*Department of Intelligent Systems Engineering, Indiana University, Bloomington, Indiana 47405, USA*
[6]*Department of Civil and Systems Engineering, Johns Hopkins University, Baltimore, Mariland 21218, USA*
[7]*Institute of Mechanics of Materials, Ruhr-University Bochum, Bochum, 44721, Germany*
[8]*Department of Aerospace and Mechanical Engineering, University of Notre Dame, Notre Dame, Indiana 46556, USA*
[9]*Computer and Computational Sciences Division, Los Alamos National Laboratory, Los Alamos, New Mexico 87545, USA*
[10]*Department of Civil and Environmental Engineering, University of Illinois, Urbana, Illinois 61801, USA*
[11]*Department of Aerospace and Mechanical Engineering, University of Notre Dame, Notre Dame, Indiana 46556, USA*
[12]*Constructora Moyeda, Monterrey, México*
[13]*Department of Civil and Environmental Engineering, Vanderbilt University, Nashville, Tennessee 37235, USA*
[14]*Department of Civil Engineering and Engineering Mechanics, Columbia University, New York, New York 10027, USA*

*Address all correspondence to: Tamar Schlick, Department of Chemistry, New York University, New York, New York 10003 USA; Tel.: (+__)_____, Fax: (+__)_____, E-mail: schlick@nyu.edu

Original Manuscript Submitted: xx/xx/20xx; Final Draft Received: xx/xx/20xx

Modeling and simulation have quickly become equivalent pillars of research along with traditional theory and experimentation. The growing realization that most complex phenomena of interest span many orders of spatial and temporal scales has led to an exponential rise in the development and application of multiscale modeling and simulation over the past two decades. In this perspective, the associate editors of the International Journal for Multiscale Computational Engineering *and their co-workers illustrate current applications in their respective fields spanning biomolecular structure and dynamics, civil engineering and materials science, computational mechanics, aerospace and mechanical engineering, and more. Such applications are highly tailored, exploit the latest and ever-evolving advances in both computer hardware and software, and contribute significantly to science, technology, and medical challenges in the 21st century.*

KEY WORDS: *?*

1. INTRODUCTION

Our world is fundamentally multiscale. Relevant phenomena span the gamut of atomic physics to evolutionary biology and astrophysics. Multiscale models and simulations allow us to probe the various spatial and temporal features of molecules, organs, materials, networks, populations, nuclear reactors, and much more with growing precision and reliability. Both software (algorithms) and hardware (parallel and distributed computers, graphics processors, cloud computing, etc) have been instrumental in making the computational time advances needed to tackle real-life complex problems (Schlick and Portillo-Ledesma, 2021). Moreover, human ingenuity/intuition together with growing data resources have allowed us to implement machine-learning and artificial-intelligence techniques as part of these multiscale model and simulation programs in many fields as never before. There is no doubt that the role of multiscale modeling and simulation will only increase in the coming years. It warrants an academic discipline in its own right, on par with basic sciences.

While aspects of multiscaling have existed for decades (see, for example, the biomolecular section below), the exponential rise of the discipline has been notable only in the past 20 years. Using the query search words "multiscale" and "multiscaling" in the SCOPUS database (within the title, key words, and abstract of the article), we obtain a clear picture of this tremendous growth. Figure 1 shows the volume of these multiscale papers (left) and the citation-weighted volume of these papers (right) per year, indicating a sharp rise since 2005, with slopes of marked increases around 2004 and again in 2012. A dissection of these papers into the 20 disciplines and scientific journals with the most papers in Fig. 2 shows engineering leading the way, followed by computer science, physics and astronomy, materials science, mathematics, earth and planetary science, chemistry, environmental science, biochemistry/molecular biology, chemical engineering, and medicine. The decomposition by journals where these multiscale papers reside indicates top representatives in *Proceedings of SPIE (International Society of Optical Engineering)*, *Lecture Notes in Computational Science & Engineering*, *Computational Methods in Applied Mechanics & Engineering*, *Journal of Computational Physics*, and *Multiscale Modeling & Simulation*. The next six journals that are close to one another in paper volume include *International Journal of Numerical Methods & Engineering*, *AIP Conference Proceedings*, *Journal of Chemical Physics*, *IEEE Transactions on Image Processing*, *Geophysics Research Letters*, and our own *International Journal for Multiscale Computational Engineering (IJMCE)*.

In this perspective article, the associate editors of *IJMCE* and their co-workers illustrate the value of multiscaling in their respective fields, from biology to mechanics and material design, providing a glimpse into important applications today, and both the algorithms and computer hardware that play a significant role in their success.

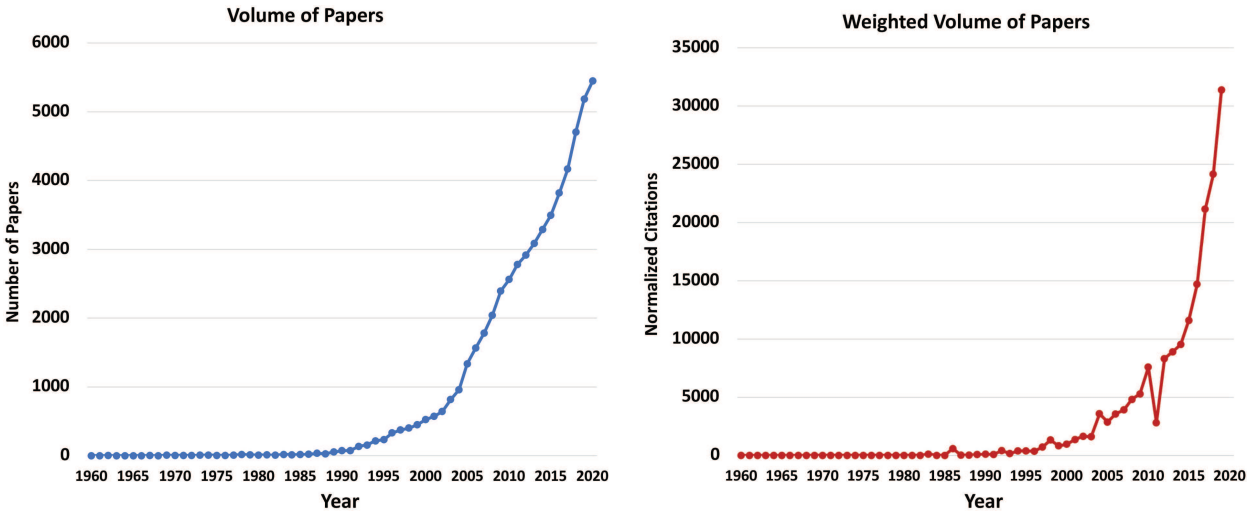

FIG. 1: The volume of papers and citation-weighted papers from the SCOPUS database with the query words "multiscale" or "multiscaling" in article title, key words, and abstract

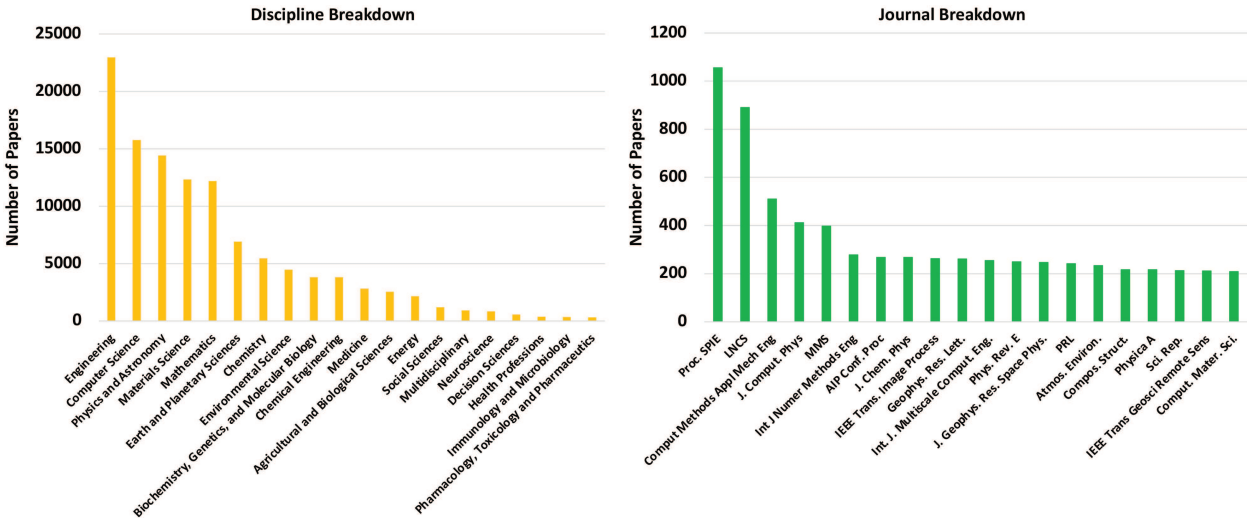

FIG. 2: The 20 scientific disciplines and journals associated with most of the multiscale papers in Fig. 1

2. MULTISCALING IN BIOMOLECULAR MODELING AND SIMULATION (T.S AND S.P.-L.)

2.1 Biological, Temporal, and Spatial Scales

Several years ago, the Department of Energy held a workshop to discuss *Scientific Grand Challenges: Opportunities in Biology at the Extreme Scale of Computing* (Schlick and Department of Energy, 2010). As a member of the panel discussing these important issues, T.S. recalls the excitement in the biological community as we discussed in 2009 how computer science and telecommunication disciplines were advancing to produce transformational technologies with far-reaching impact on science, society, and human health. There is no better time to realize these key influences as we enter the second year of the Covid-19 pandemic that has altered almost every aspect of our lives. Indeed, the anticipated breakthroughs from the marriage of the biosciences and powerful cyberinfrastructures have been realized by the enormous impact of predictive modeling, medical technology, and vaccine development in warp speed. Many of these developments were made possible by multiscale modeling, required to study the structures, motions, and functions of large biophysical systems such as viral RNAs and viral proteins in their complex cellular milieu [see Introduction in Schlick et al. (2021b)].

As illustrated in Fig. 1 in the DOE report, reproduced here in Fig. 3, biological system sizes span from thousands of atoms in proteins, RNAs, and other macromolecules to the order of 10^{10} atoms in whole cells. The associated relevant timescales of motion range from femtoseconds to minutes and longer. This requires appropriate reduction, approximation, and integration of modeling at different levels. Bridging these scales requires connections that telescope the findings from one level to the other, so that we simulate the functional dynamics associated with those systems, investigate processes involving many biomolecules, and pursue the cellular implications of these processes. Algorithms such as enhanced sampling, data science tools like trajectory management and visualization, and exascale hardware facilities play crucial roles in these multiscale approaches.

The DOE report highlights how the functioning of biological nanomachines that take part in the basic processes of life can be divided into four categories of increasing spatial/temporal complexity: *protein folding and RNA folding*; *biochemical binding and reaction mechanisms*, such as enzyme catalysis and protein/ligand interactions; *macromolecular pathways*, including DNA replication and repair fidelity, protein synthesis, chromatin organization, and RNA editing; and *supramolecular cellular processes*, such as protein signaling networks, plant cell-wall formation, and endocytosis. Separable tools that "admit a variety of time, space, and trajectory sampling methods (and fully exploit the hundreds of millions of cores expected on an exascale machine) will enable long time integrations, implicit solvation conditions, and mixed molecular mechanics and quantum mechanics models" (Schlick and Department of Energy, 2010).

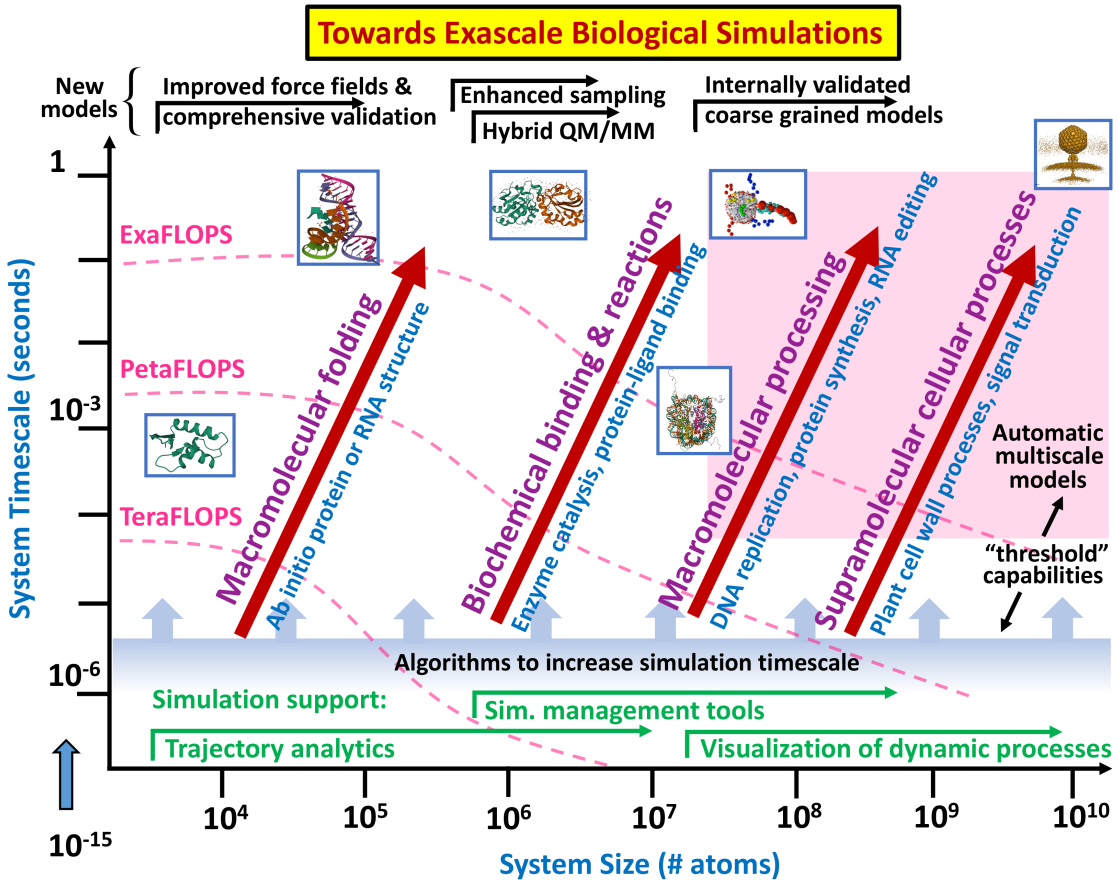

FIG. 3: Multiscale areas relevant to biology. Reproduced from the 2009 DOE report Schlick and Department of Energy (2010)

The most challenging aspect of modeling biomolecules is that all these motions on different spatial and temporal scales are intimately coupled. This makes many approaches like implicit integration methods in chemical kinetics inadequate because the fast processes are not decaying but rather oscillatory. This has been the problem mainly known as the timescale problem in molecular dynamics integration (Schlick, 2010). Although some integration approaches for molecular dynamics have helped alleviate the severe timestep requirement for biomolecular dynamics integration, the real improvement has come from both hardware advances and coarse-grained/multiscale models. In the latter, rather than treating individual atoms, groups of atoms are modeled. This simplification facilitates the molecular representation but also requires development of new force fields for these reduced-atom models. This multiscale approach was first described in computational biology with simplified protein models and hybrid molecular mechanics/quantum-mechanical models for chemical reactions that were recognized in the 2013 Nobel Prize in Chemistry awarded to Martin Karplus, Michael Levitt, and Arieh Warshel [see Schlick (2013), for an article on the significance of this award for computational biology]. Interestingly, machine-learning approaches are now replacing the computationally expensive quantum-mechanics component.

2.2 Coarse-Grained Models

Many coarse-grained and multiscale models of biological systems are used today, including for proteins, RNAs, DNAs, membranes, and other biomolecules, as described in two recent perspectives—Schlick and Portillo-Ledesma (2021) and Schlick et al. (2021a). While coarse-grained models involve a simplified representation of the system, multiscale models integrate different levels of the system. An example of the former is a graph-theory representation

to coarse grain RNAs as graphs, with important applications to the frameshifting RNA element of the Covid-19 RNA (Schlick et al., 2021b,c). By representing RNAs as graphs, the conformational space is vastly reduced from sequence space to motif space. As motif space grows much more slowly with RNA size than sequence space, graph representations allow systematic exploration of motifs for design of novel RNA motifs and mutations. This feature was exploited in recent computations of motif-altering minimal mutations of the frameshifting element of the SARS-CoV-2 viral genome to define targets for antiviral drugs or gene editing (Schlick et al., 2021b,c). Two examples of multiscaling include a model for the SARS-CoV-2 virion, which includes the outer protein coat and its membrane (Yu et al., 2021) and the multiscale chromatin model described below.

2.3 Multiscale Chromatin Model

Genome organization is a fascinating area of biology/biophysics which necessitates development of models on many scales to study and bridge experimental data obtained from the chromatin fiber to chromosomes. In the cell nucleus of eukaryotic systems, one billion base pairs are compressed into a polymeric complex associated with chromosomal DNA, which has many levels of organization and features that we are just beginning to understand (see Fig. 4). The condensation required spans many orders of magnitude to fit meters-long DNA when stretched into a cell nucleus of micron diameter. This enormous condensation is achieved through formation of the chromatin fiber that makes up chromosomes.

The DNA base pairs that define up genomes are wound around protein cores like yarn around many spools to form the *chromatin fiber*. At low salt, this nucleic acid/protein fiber is an open "beads-on-a-string" type polymer, but at certain cell states it condenses greatly with the aid of auxiliary and remodeling proteins to form highly condensed and folded states (Kornberg, 1977). At the kilobase level, or secondary structure of chromatin, zigzag topologies are recognized, with self-associating fibers that have strong second-neighbor nucleosome connections (Grigoryev et al., 2016). These arrangements are heterogeneous with variable sizes, as expected from a floppy polymer in solution (Ou et al., 2017). At the level of megabases of DNA base pairs, these chromatin assemblies form loops and compartment domains that have unique functional roles associated with specific genes (Lieberman-Aiden et al., 2009). The chromatin fiber also displays various levels of condensation within the cell nucleus, for example, relatively open euchromatin and condensed heterochromatin (Eagen et al., 2015). Furthermore, individual chromosomes are known

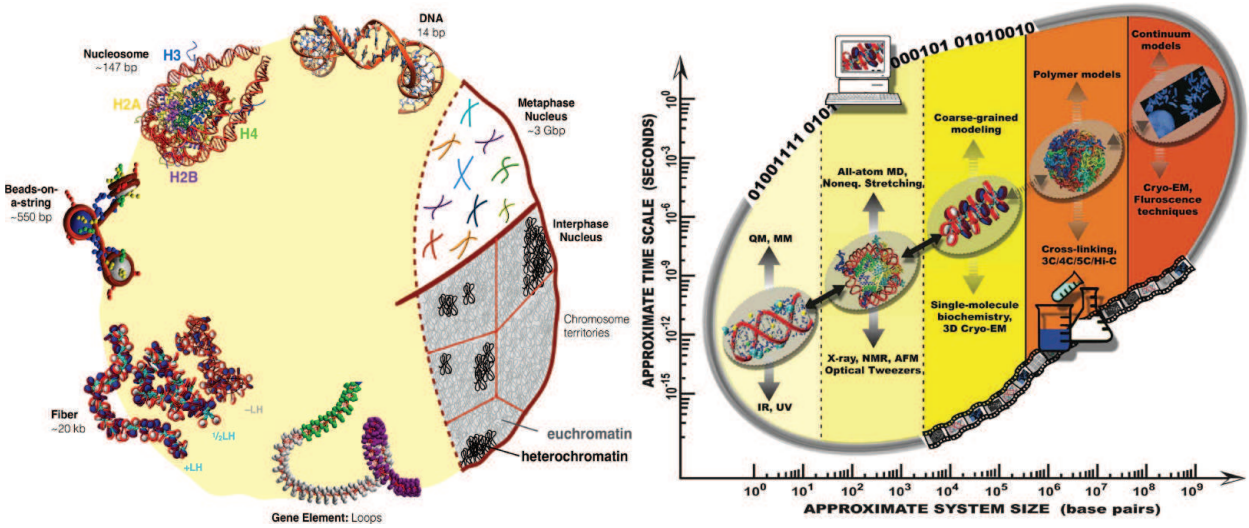

FIG. 4: The DNA folding problem. (Left) In eukaryotic cells, the DNA wraps around nucleosomes to form fibers, genes, and chromosomes, at various levels of condensation, taken from Bascom and Schlick (2017). (Right) The different levels of DNA folding can be studied by a variety of computational and experimental tools, but connection strengths (arrow color) are weaker for some levels and along the upper diagonal arrow, taken from Ozer et al. (2015).

to occupy distinct territories in the cell nucleus (Speicher and Carter, 2005). We are only beginning to understand how these transitions from open to highly condensed states occur and how they are regulated by the cellular machinery (Maeshima et al., 2020; Rowley and Corces, 2018). These different open and condensed states and associated transitions are key, because all transcript-directed processes involving DNA require the DNA to be accessible to the cellular machines and hence unraveled.

Over the past two decades, our group has developed an increasingly complex multiscale model of chromatin to study genome properties at the fiber and gene levels (Bascom et al., 2018; Portillo-Ledesma and Schlick, 2020). As new experimental data have become available, for example, regarding histone tails or linker histone asymmetry, these features have been incorporated into our model, shown in Fig. 5.

The model combines different levels of coarse-graining. The DNA that connects the core nucleosome units is coarse grained by beads, each of which represents about nine basepairs of double helical DNA. Coarse-grained protein beads with a resolution of about five amino acids per bead are used to represent the flexible histone protein tails and the linker-histone protein beads. These DNA and protein beads are then combined with an electrostatically charged irregular surface approximation (Beard and Schlick, 2001) for the nucleosome core based on the crystal structure so that each of the approximately 300-point charges can be used to collectively reproduce the electrostatic properties of the atomistic nucleosome core particle. These units are combined, with experimental anchoring for the relative positioning so that each bead and core has an associated Euler body-faced coordinate frame. These geometries are used to compute the coordinates and energies of the system. The potential energy includes stretching, bending, twisting, electrostatic, and exclusion-volume components. The conformational space of this complex system is then sampled using equilibrium Monte Carlo, with local and global rotation and translational moves. Recently, Brownian dynamics sampling has been added as well, allowing path sampling for small chromatin systems. A multiscaling strategy was also used to incorporate the effects of epigenetic marks (Collepardo-Guevara et al., 2015).

In Fig. 6 we illustrate some recent biological applications of our chromatin model. These include formation of nucleosome clutches, or groups of nucleosomes, during cell differentiation (Gómez-García et al., 2021; Portillo-Ledesma et al., 2021); epigenetic effects of histone tail acetylation on fiber openings (Collepardo-Guevara et al., 2015); domain segregation in fibers composed of alternating acetylated and wildtype tails (Rao et al., 2017); and the effect of linker-histone reduction on tumorigenic progression of lymphoma cells (Yusufova et al., 2021).

The clutch study compares clutch patterns of uniform chromatin fibers that vary in the levels of acetylation, linker histone density, and the position of nucleosomes to those of fibers that mimic a gene related to mouse development. It dissects the role of each chromatin parameter in clutch regulation, indicating that a delicate combination of these three parameters produces larger clutches upon differentiation [Fig. 6(a)] (Gómez-García et al., 2021; Portillo-Ledesma et al., 2021).

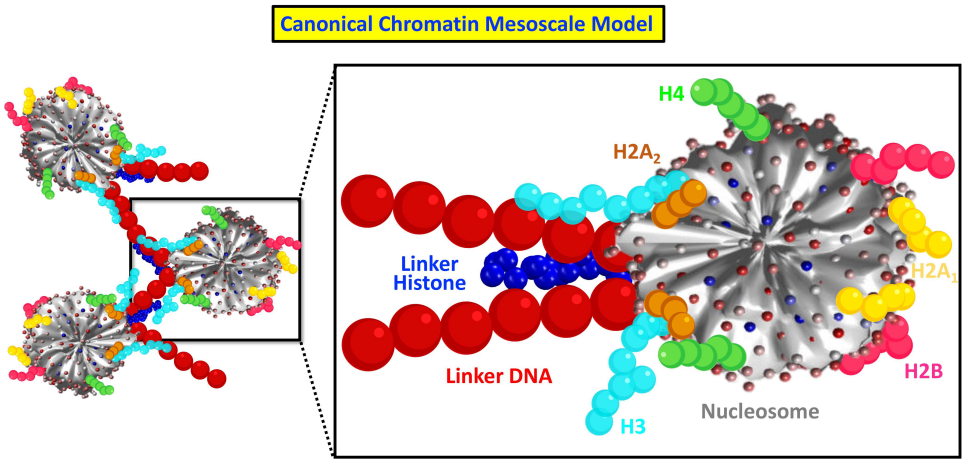

FIG. 5: Mesoscale chromatin model. Coarse-grained beads for the DNA linkers, flexible histone tails, and linker-histone units are combined with a charged irregular surface model for the nucleosome core.

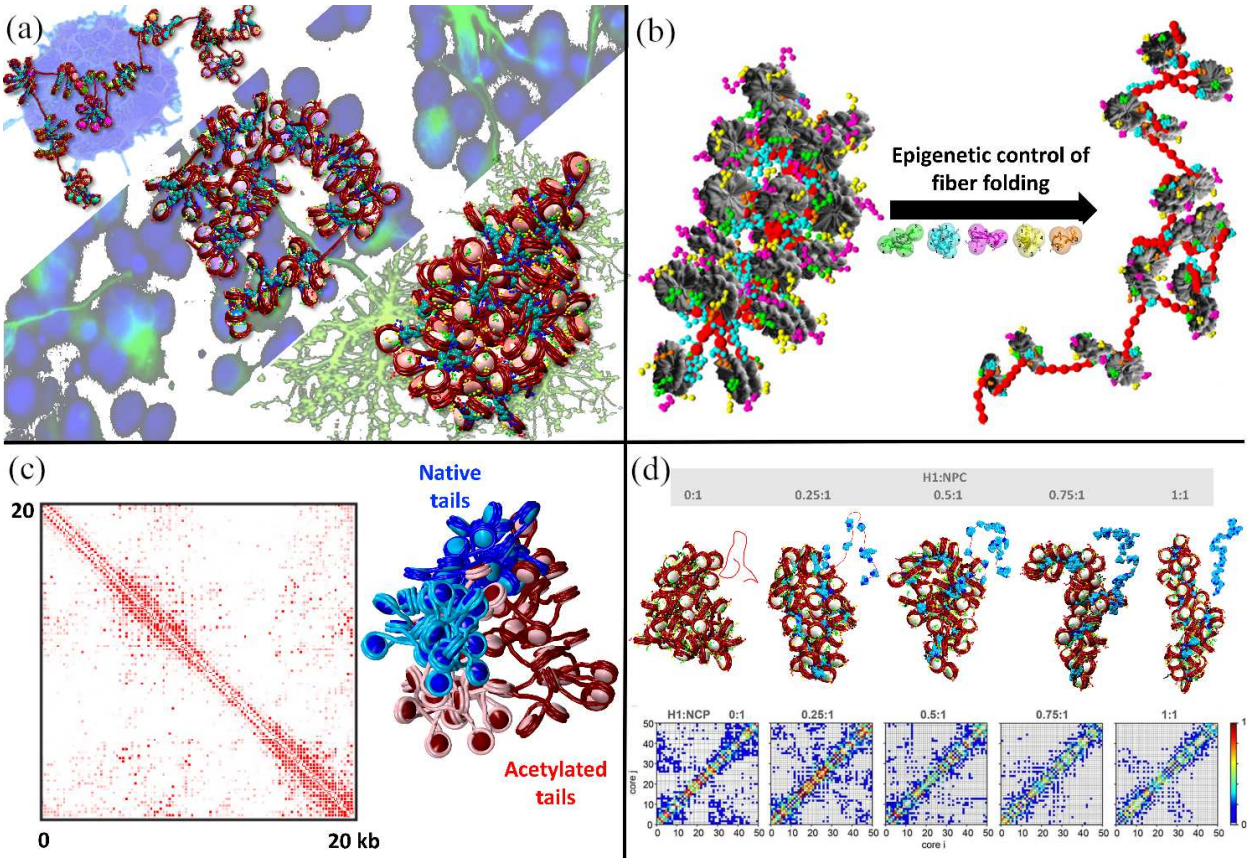

FIG. 6: Recent mesoscale chromatin model applications. (a) The differentiation state of the cell is correlated to clutch patterns, as illustrated here for neural cells at increasing differentiation from top to bottom (Portillo-Ledesma et al., 2021). (b) Chromatin unfolds upon including acetylated tails in the chromatin mesoscale model (Collepardo-Guevara et al., 2015). (c) Chromatin compartmentalization is directed by the interactions between same-type tails (Rao et al., 2017). (d) A loss of linker histone produces a looser fiber that can be easily transcribed, up regulating certain genes (Yusufova et al., 2021).

Notably, in the acetylation studies another level of multiscaling is utilized, where results of atomistic simulations of dinucleosomes with acetylated tails are incorporated into the mesoscale chromatin model using more rigid tail conformations with altered force constants (Collepardo-Guevara et al., 2015). Fibers with acetylated tails unfold due to an impairment of the stabilizing internucleosome interactions [Fig. 6(b)], highlighting the role of these epigenetic modifications in regulating chromatin openings (Rao et al., 2017). When these rigid tails are used to construct fibers with alternating acetylated and wildtype tails, segregated nucleosome camps result, producing a "checkerboard" nucleosome contact matrix [Fig. 6(c)]. Thus, epigenetic marks lead to chromatin segregation on this scale, connecting local to global structure.

In the linker-histone study, fibers modeled with different linker-histone densities explain the architectural chromatin changes that lead to lymphoma upon linker-histone loss. Lower linker-histone densities produce a transition from a straight and rigid structure, with almost no long-range interactions, to a loose and flexible fiber that can be easily transcribed, increasing the expression of genes that should be silenced [Fig. 6(d)] (Yusufova et al., 2021).

Such combinations of coarse-graining and multiscaling will need to be combined and developed in new ways in the future to tackle problems on higher scales of genome organization and to understand chromatin loops on the megabase level and chromosomal domains. At present, many simple polymer models are being applied to study chromosomal arrangements, but these cannot include key internal and external parameters of chromatin fibers, such as linker-histone densities, irregularly nucleosome positions, acetylation islands, and so on, which are crucial to

interpret chromatin structure and function from first principles. Our challenge will be to develop ways to achieve both inclusion of relevant local parameters and achievement of large-scale views. Connecting these many levels will require innovative ways of multiscaling.

3. ELECTRO-MECHANICAL MULTISCALE MODELING OF CANCELOUS BONE (M.B. AND K.H.)

Multiscale modeling is also important for simulating bones, which are subjected to mechanical, electrical, and magnetic effects. An important medical application of this model is the use of sonography as a noninvasive diagnosis tool for the early detection of osteoporosis (Kaufman et al., 2008), a bone disease that weakens the bone, increasing the likelihood of fractures.

In recent decades, scientists with different backgrounds who studied bone material developed different approaches to simulate bone behavior. Scientifically, bone is an interesting material with impressive properties. It is strong and possesses a high stiffness and fracture toughness, while also maintaining a light weight (Hamed et al., 2010). As a composite material, cancelous (spongy) bone consists of small beams or shells of interconnected cortical bone and interstitial bone marrow. Thus cancelous bone possesses a very complex and heterogeneous microstructure, ideal for multiscale modeling.

We employ the finite element square method (FE^2), which extends the standard finite element method (FEM) by applying the multiscale concept and solving the differential equation systems on two scales via the FEM. See method overview in Miehe et al. (1999) and Schröder and Hackl (2013). Examples from the domains of biomechanics and electromechanics are given in Chapelle et al. (2012) and Vallicotti et al. (2018). Applications of the FE^2 within the scope of bone modeling can be found in Biswas et al. (2019), Gilbert et al. (2007), Pahr and Zysset (2008), and Ilic et al. (2010). Instead of including microheterogeneities directly, which would require an extremely fine mesh resolution, a second, smaller scale is introduced to solve the problem. Assuming the material is statistically regular on the smaller scale, it can be modeled by a corresponding representative volume element (RVE). Here we denote the larger scale as the macroscale and the smaller scale as the microscale. For the calculations, instead of using a macroscopic material model, the state variables are assigned as microscale, where they are used to solve the RVE problem. These microscale calculations then yield average flux quantities and consistent tangent matrices for the solution of the macroscale problem.

While past research often focused only on the mechanical properties of bone, our model includes the complete coupling of electrical and magnetic effects as well. Cortical bone is mainly composed of elastic collagen fibers acting as charge carriers. When a shear stress is applied, these collagen fibers slip past each other, thus producing the piezoelectric effect (Fukada and Yasuda, 1957). This means that whenever a mechanical strain is present in the bone, an electric field is generated due to the piezoelectric effect. A time-dependent fluctuation of the electric field then creates a magnetic field due to Ampère's circuital law, coupling mechanical, electrical, and magnetic effects together. For our modeling we assume a heterogenous material consisting of two phases, cortical bone and bone marrow.

As stated above, an important application of bone modeling is the early detection of osteoporosis. Compared to a healthy bone, the volume fraction of cortical bone for a degenerated bone can be reduced from 30% to 5% (Ilic et al., 2010; Steeb, 2010). Figure 7 shows a comparison depending on the osteoporosis stage and illustrates the heterogeneity of the material. During the course of osteoporosis, the cortical bone (represented brighter) reduces and is replaced by bone marrow (represented in dark). Thus we will employ different RVEs for the simulations. Here the cortical bone phase is represented in gray, while the bone marrow phase is drawn in transparent red color.

Early detection of osteoporosis can be done via sonography: ultrasonic waves enter the bone and due to the described effects create a magnetic field, which can be measured (Güzelsu and Saha, 1981). Depending on the results, conclusions on the health status of the investigated bone can be drawn.

We model bone as a heterogenous material consisting of two phases, cortical bone and bone marrow, see Blaszczyk and Hackl (2021a,b). Cortical bone is modeled as piezoelectric, insulating solid bone marrow as viscoelastic, conducting solid. Electrical and magnetic effects are coupled via the Maxwell equations. Based on energy methods in mechanics, we establish a thermodynamically consistent material model and derive the weak and strong form of the corresponding boundary-value problem. We split the domain $\Omega := \Omega_{\mathbf{y}}$, representing the RVE of the micro problem, into a cortical bone part Ω_{b} and a bone marrow part Ω_{m}. For any quantity, the indicies $(\cdot)_{\mathrm{m}}$ and

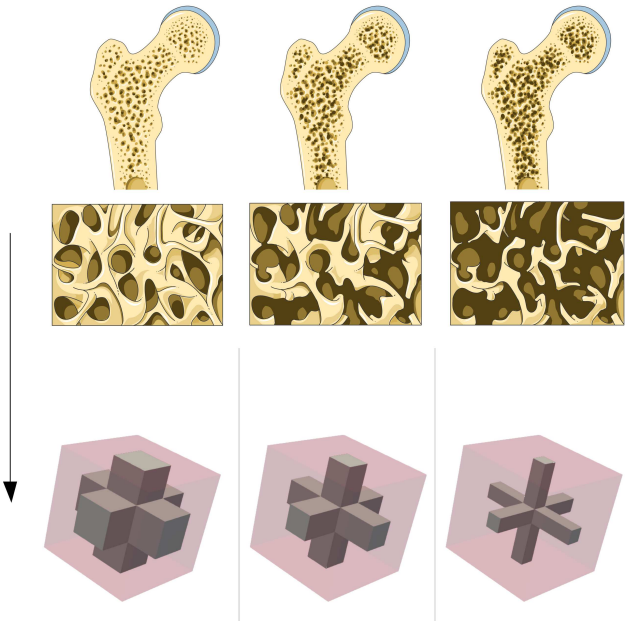

FIG. 7: Bone phases depending on osteoporosis stage (cf. Laboratoires Servier, 2019) and corresponding RVEs

$(\cdot)_\mathrm{b}$ are used to denote the affiliation to each phase. If no index is present, the quantity or equation is valid for both phases.

We employ a thermodynamic energy functional at the microscale, which contains the energy densities Ψ_b and Ψ_m of both phases, a volume constraint $\mathcal{C}$, dissipation and gauge functionals (Δ and Ψ_g), and the potential of the generalized external forces W_ext. The main variables of the problem are then the mechanical displacements $\mathbf{u}$, the electric scalar potential φ, and the magnetic vector potential $\mathbf{A}$, yielding seven unknown variables for the three-dimensional model. The state variables are the mechanical strain $\boldsymbol{\varepsilon}$, the electric field $\mathbf{E}$, and the magnetic flux density $\mathbf{B}$, which can be calculated from the main variables. Then two of the four Maxwell equations are already satisfied.

The energy densities for both phases consist of quadratic energies for mechanical, electrical, and magnetic effects, resulting in a linear problem. We include a piezoelectric energy term for the cortical bone phase. For the bone marrow phase, an inelastic strain $\boldsymbol{\varepsilon}^i$ and the viscosity parameter μ_v^{-1} are introduced. The constraint function enforces volume conservation of the inelastic deformation. The dissipation function governs the evolution of the inelastic strain and the energy loss due to conduction, which both occur only in the bone marrow phase. The gauge function ensures that a unique solution for the magnetic vector potential $\mathbf{A}$ is obtained by penalizing its divergence, effectively requiring that $\nabla \cdot \mathbf{A}$ vanishes and thus improving the numerical stability (Semenov et al., 2006). The penalty parameter γ is a numerical parameter used to control the gauge term. Finally, the potential of generalized external forces contains $\mathbf{f}$ and $\mathbf{t}$, the mechanical volume and surface forces, q_v and q_s, the electric volume and surface charges, and $\mathbf{j}_\mathrm{v}$ and $\mathbf{j}_\mathrm{s}$, the volume and surface currents. By calculating the derivative of the energy density with respect to the state variables, we find the constitutive equations, from which we calculate the material tensors $\mathbb{C}$ (mechanical stiffness tensor), $\boldsymbol{\xi}$ (permittivity tensor), $\boldsymbol{\mu}^{-1}$ (inverse permeability tensor), $\mathbf{e}$ (piezoelectric tensor), and $\boldsymbol{\kappa}$ (electric conductivity tensor). We derive the flux quantities mechanical stress $\boldsymbol{\sigma}$, electric displacement $\mathbf{D}$, magnetic field strength $\mathbf{H}$, and the electric current density $\mathbf{J}$. For the cortical bone phase, the viscosity parameter μ_v^{-1} and the electric conductivity tensor $\boldsymbol{\kappa}$ vanish.

We use the stationary condition of the energy functional to calculate the weak and strong form of the problem. The weak form is later used to apply the FEM. For the strong form, we obtain the mechanical equilibrium condition, the two remaining Maxwell equations, and boundary conditions, including the gauge. Additionally, we receive the jump conditions between the phases on the interface $\partial\Omega_\mathrm{bm}$ and the evolution equation of the inelastic strain. The time integration of the evolution equation is achieved by applying the explicit Euler method.

To connect the macro- and microscale in FE^2, it is important to discuss the transition between the scales. The Hill–Mandel conditions (Hill, 1963) have to be fulfilled, guaranteeing energy conservation during the scale transition, i.e., the virtual work on the macroscale has to be equal to the virtual work on the microscale.

For the macro-to-micro transition, we fulfill these conditions by using periodic boundary conditions on the microscale, as they are the only type of boundary condition where the results on the microscale are independent from the relative geometry of the RVE (Schröder and Hackl, 2013). Additionally, as the RVE is periodic in space, this type of boundary condition is the most suitable (Ilic et al., 2010). The micro state variables consist then of two parts: a term resulting from the microscopic main variables [denoted by $\tilde{(\cdot)}$], whose fluctuations are calculated, and a term contributed by the macroscale:

$$\boldsymbol{\varepsilon} = \tilde{\boldsymbol{\varepsilon}}(\mathbf{y}) + \overline{\boldsymbol{\varepsilon}}(\mathbf{x}), \quad \mathbf{E} = \tilde{\mathbf{E}}(\mathbf{y}) + \overline{\mathbf{E}}(\mathbf{x}), \quad \text{and} \quad \mathbf{B} = \tilde{\mathbf{B}}(\mathbf{y}) + \overline{\mathbf{B}}(\mathbf{x}). \tag{1}$$

This way we calculate the flux variables on the microscale. For the micro-to-macro transition, the volume average of these flux quantities is sent back to the macroscale:

$$\begin{gathered}\overline{\boldsymbol{\sigma}}(\mathbf{x}) = \frac{1}{\Omega}\int_{\Omega} \boldsymbol{\sigma}(\mathbf{y})\mathrm{d}V, \quad \overline{\mathbf{D}}(\mathbf{x}) = \frac{1}{\Omega}\int_{\Omega} \mathbf{D}(\mathbf{y})\mathrm{d}V, \quad \dot{\overline{\mathbf{D}}}(\mathbf{x}) = \frac{1}{\Omega}\int_{\Omega} \dot{\mathbf{D}}(\mathbf{y})\mathrm{d}V, \\ \overline{\mathbf{H}}(\mathbf{x}) = \frac{1}{\Omega}\int_{\Omega} \mathbf{H}(\mathbf{y})\mathrm{d}V, \quad \text{and} \quad \overline{\mathbf{J}}(\mathbf{x}) = \frac{1}{\Omega}\int_{\Omega} \mathbf{J}(\mathbf{y})\mathrm{d}V.\end{gathered} \tag{2}$$

Additionally, in this model energy dissipation is considered in two ways. For the electric current $\mathbf{J}$, the average is calculated and included in the scale transition, resulting in no energy loss during the scale transition. For the inelastic strain $\boldsymbol{\varepsilon}^i$, the complete state in every point and for every RVE is saved. Thus the dissipation occurs only on the microscale and the energy conservation is fulfilled, as the virtual work send to the microscale is equal to the virtual work send back added to the energy dissipation on the microscale. With the flux variables available on the macroscale, it is now possible to obtain the macro residual for the Newton–Raphson method and the calculation of consistent macro tangent moduli remains, which are needed for the iteration.

The calculation is performed by applying a small numerical perturbation $\Delta_{\mathrm{tol}} = 10^{-8}$ to each entry of the corresponding state variable and then calculating each entry of the macroscopic tangent tensors by evaluating the perturbed fluxes $\overline{\boldsymbol{\sigma}}^{p_i}, \overline{\mathbf{D}}^{p_i}, \overline{\mathbf{H}}^{p_i}, \overline{\mathbf{J}}^{p_i}$ by means of the RVE. Since for our model the same RVE is used everywhere and the nonlinearity from the inelastic strain is very small, this calculation has to be done only once for all RVEs and all time steps, making this approach very efficient. Together with the calculated macro state variables, this allows the macroscopic FE problem to be solved.

We use the same parameters for both scales. Here the time-step increment is $\Delta_{\mathrm{t}} = 1 \times 10^{-3}$ s, the Newton–Raphson tolerance is $\mathrm{tol}_{\mathrm{N}} = 1 \times 10^{-8}$, and the gauge penalty parameter is $\gamma = 1.0\ \mathrm{s^2A^2/(kg\,m)}$.

The default material parameters used are shown in Table 1. Young's modulus and Poisson's ratio for both phases can be found in Steeb (2010). All other parameters are of a rather academical nature and influence the results only

TABLE 1: Default material parameters

Material parameter		**Cortical bone**		**Bone marrow**	
Young's modulus	E	22.0	GPa	2.0	GPa
Poisson's ratio	ν	0.32	—	0.3	—
Permittivity	ξ_1	8.85×10^{-12}	F/m	8.85×10^{-12}	F/m
Permeability	μ_{c}	1.257×10^{-6}	H/m	1.257×10^{-6}	H/m
Piezoelectric coefficient	e_{15}	3.0×10^{-3}	A s/m^2	0	A s/m^2
Electric conductivity	κ_1	0	S/m	1.0×10^4	S/m
Viscosity parameter	μ_{v}	0	s/GPa	$5.0 \times \Delta_t$	s/GPa

marginally. We assume linear isotropic material everywhere, excluding the piezoelectric tensor, which is preferential in the z-axis due to the longitudinal orientation of the collagen fibers.

We restrict ourselves to microscale simulations. For our first example, we use a degenerated bone RVE with $\rho_\mathrm{b} = 5.3\%$. We compare different mesh resolutions. The first RVE consists of six elements for each spatial direction. The second RVE consists of 12 elements for each spatial direction. We apply a macroscopic strain $\varepsilon_{yz} = 1 \times 10^{-5}$. Figure 8(a) shows the results of the simulations.

Both simulations show quadratic convergence behavior and periodic results. For both quantities, the results between the two different used meshes look nearly identical, confirming mesh independence of the results.

To compare periodic RVEs for different stages of osteoporosis, we created six different RVEs with the same total volume of $V_\mathrm{RVE} = 1$ mm^3 and $\rho_\mathrm{b} \in \{5.3\%, 10.4\%, 14.5\%, 19.1\%, 24.2\%, 29.5\%\}$. The macroscopic mechanical stiffness tensor $\overline{\mathbb{C}} := \partial\overline{\boldsymbol{\sigma}}/\partial\overline{\boldsymbol{\varepsilon}}$ was now evaluated for all RVEs by applying a small numerical perturbation. Then we calculate the effective Young's modulus as

$$E_\mathrm{eff} = \frac{\overline{\mathbb{C}}_{44}\left(3\overline{\mathbb{C}}_{12} + 2\overline{\mathbb{C}}_{44}\right)}{\overline{\mathbb{C}}_{12} + \overline{\mathbb{C}}_{44}}. \tag{3}$$

Figure 8(b) shows a plot of the macroscopic Young's modulus against the volume fraction of cortical bone. Here we observe a drastical reduction of the macroscopic Young's modulus with decreasing cortical bone fraction. Compared to a healthy bone ($\rho_\mathrm{b} = 29.5\%$), the effective Young's modulus of the degenerated bone ($\rho_\mathrm{b} = 5.3\%$) decreases to 57% (from 3.89 to 2.32 GPa). Similar results can be found in Ilic et al. (2010).

As a second example, we performed multiscale simulations on a true-to-scale model of a human femur bone. Here we applied a time-dependent mechanical displacement with amplitude $u_\mathrm{max} = 2 \times 10^{-6}$ to the middle section of the bone and calculate 100 timesteps ($\Delta_\mathrm{t} = 1 \times 10^{-2}$ s), comparing the degenerated bone (RVE 1, $\rho_\mathrm{b} = 5.3\%$) to the healthy bone (RVE 6, $\rho_\mathrm{b} = 29.5\%$). Figures 9 and 10 show the results of the simulations. All quantities drastically decrease for the degenerated bone. Compared to the healthy bone, the average magnetic field strength for the degenerated bone reduces to only about one-third.

Our fully coupled multiscale model of cancellous bone considered mechanical, electrical, and magnetic effects. Both micro- and multiscale simulations yield good results. By using the FE^2, we were able to perform multiscale simulations of a true-to-scale human femur bone model, which can help to better understand experimentally observed time effects on bone. For future research we aim to solve the inverse problem—recovery of the distribution of cortical bone phase from magnetic field data—by using an artificial neural network to predict simulation outputs. Additionally, wave propagation in cancellous bone will be investigated.

4. STABILIZED AND VARIATIONAL MULTISCALE METHODS FOR MULTIPHYSICS PROBLEMS (A.M.)

Advances in computational resources have made numerical simulations an indispensable tool across engineering and sciences. Of great contemporary interest are problems that are governed by multiple coupled partial differential

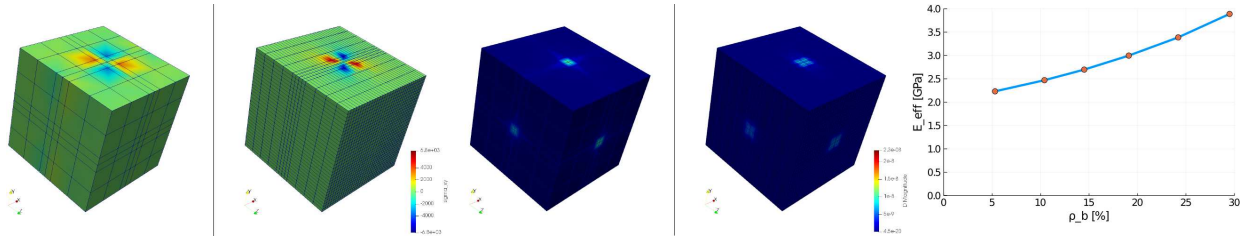

(a) (b)

FIG. 8: Microscale simulation results of a coarse and fine mesh (left and right resp.) (a) Left: σ_{xy} [GPa], right: $\mathbf{D}$ [A s/m^2]. Effective Young's modulus E_eff against cortical bone volume fraction ρ_b for different RVEs (b).

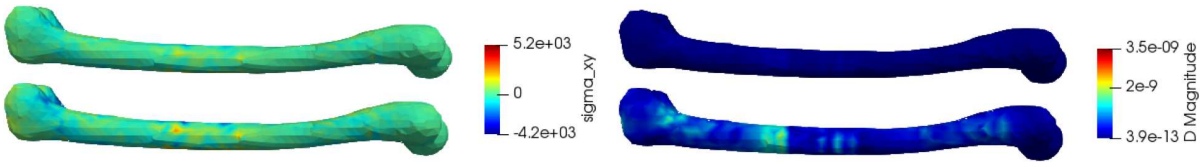

(a) (b)

FIG. 9: Simulation results of the femur bone model for the degenerated (top) and healthy RVE (bottom), $t = 25$. Left: σ_{xy} [GPa], right: $\mathbf{D}$ [A s/mA s/m^2].

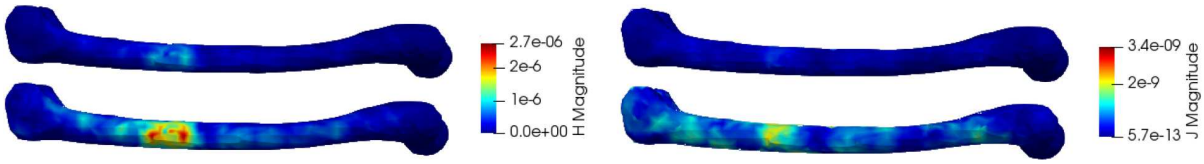

(a) (b)

FIG. 10: Simulation results of the femur bone model for the degenerated (top) and healthy RVE (bottom), $t = 50$. Left: $\mathbf{H}$ [A/m], right: $\mathbf{J}$ [A/mA s/m^2].

equations (PDEs) on overlapping and/or on adjoining subdomains. These problems are invariably multiscale because of the multiple coupled balance laws with their associated material, spatial and temporal scales. The drive for developing high-fidelity computational methods for complex multiphysics problems has led to several successful approaches. Among the various successful efforts is the development of the class of stabilized methods. The underlying philosophy of the stabilized methods is to strengthen the classical variational formulations so that discrete approximations, which would otherwise be unstable, become stable and convergent. The origins of stabilized methods can be traced back to the early 1980s, when Hughes and colleagues realized the issue of lack of stability of the Galerkin method for advection-dominated diffusion problems. To correct this deficiency in the standard Galerkin approach, the streamline-upwind-Petrov–Galerkin (SUPG) method was proposed (Brooks and Hughes, 1982). The SUPG method turned out to be the forerunner of a new class of stabilization schemes, namely, the Galerkin/least-squares (GLS) stabilization methods (Hughes and Franca, 1987). In the GLS method a least-squares form of the residuals that is based on the corresponding Euler-Lagrange equations is added to the Galerkin finite-element formulation. A general theory of the stabilized methods was developed, and success was achieved on a variety of problems. Concurrently, another class of stabilized methods that is based on the idea of augmenting the Galerkin method with virtual bubble functions, called the residual-free bubbles (RFB) approach, was introduced by Brezzi et al. (1997, 1998). In the mid 1990s, Hughes revisited the origins of the stabilization schemes from a variational multiscale viewpoint and presented the variational multiscale method (VMS) (Hughes, 1995). In this method the different stabilization techniques come together as special cases of the underlying subgrid-scale modeling concept.

The VMS method (Hughes, 1995; Hughes et al., 1998a; Masud and Franca, 2008; Masud and Hughes, 2002; Masud and Scovazzi, 2011), which is an offspring of the earlier developments of stabilized methods, is based on an underlying subgrid-scale modeling concept. The key idea in the VMS framework is to perform a mathematical nesting of the fine scales into the coarse scales, thereby providing a robust framework wherein all the important features of the total solution are consistently represented in the computed solution. It is facilitated by an *a priori* direct sum of functions into coarse- and fine-scale space. This decoupling leads to a decomposition of scales into two overlapping components that are categorized as coarse scales and fine scales, respectively.

Typically, the coarse scales are expanded via the traditional finite-element shape functions, while the fine scales that lie in an infinite-dimensional space, are defined to be the remaining part of the solution. The decoupling of the spaces of functions leads to the decomposition of the problem into two subproblems, namely, the coarse-scale subproblem and the fine-scale subproblem. The modeling aspect in the method lies in that the scale solution is then

variationally projected onto the coarse scales (see Fig. 11). Although the final formulation does not depend explicitly on the fine-scale fields, the effects of fine scales are consistently represented via the additional residual-based terms.

There are two dominant approaches to VMS methods: (i) the Green's function approach (Bazilevs et al., 2007; Codina et al., 2007; Franca et al., 2006; Hughes, 1995; Hughes et al., 1998a), and (ii) the bubble-functions approach, applied directly to the fine-scale variational equation (Masud and Calderer, 2009; Masud and Franca, 2008; Masud and Scovazzi, 2011). The Green's-function-based approach was applied successfully to stabilize fluid-flow problems and drive residual-based turbulence models (Bazilevs et al., 2007; Codina et al., 2007; Colomés et al., 2015). The latter approach, which is a generalization of the RFB method (Brezzi et al., 1997, 1998), was developed by Masud and co-workers to derive stabilized formulations for a variety of mixed field problems (Masud and Calderer, 2009, 2011, 2013; Masud and Khurram, 2004; Masud and Truster, 2013; Masudr et al., 2012). A unique feature of this class of methods is that the solution of the fine-scale variational equation does not require *a priori* assumptions on the structure of the subgrid scale. Subsequently, the hierarchical VMS framework was proposed in Masud and Franca (2008) and Masud and Scovazzi (2011), which resulted in variationally derived closure models for incompressible turbulent flows (Calderer and Masud, 2013; Masud and Calderer, 2011; Masud and Zhu, 2021), as shown in Figs. 12 and 13.

The VMS framework when viewed from the perspective of subgrade-scale physics provides a platform for variational coupling of multiple PDEs on concurrent and/or adjoining subdomains. Embedding ideas from the discontinuous Galerkin (DG) method in the bubble-enriched VMS framework, Masud and co-workers presented the variational multiscale discontinuous Galerkin (VMDG) methods (Masudr et al., 2012; Truster and Masud, 2014; Zhu and Masud, 2021) with rigorous treatment of the continuity conditions that are critical to numerical and algorithmic stability. The VMDG method facilitates variational embedding of the fine-scale interface models in a mathematically consistent fashion, admits common element types, and is free of user-defined tuning parameters (Calderer and Masud, 2013; Chen et al., 2020; Masud and Truster, 2013; Truster and Masud, 2014; Zhu and Masud, 2021). The enhanced stability of the VMDG framework enables the treatment of various interface kinematics, such as nonmatching mashes

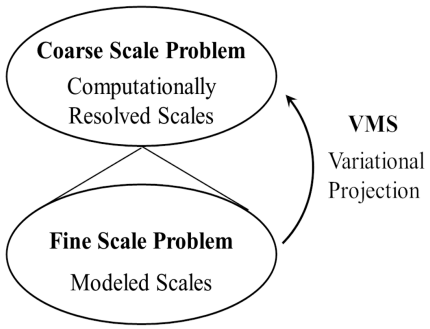

FIG. 11: Schematics of the VMS method

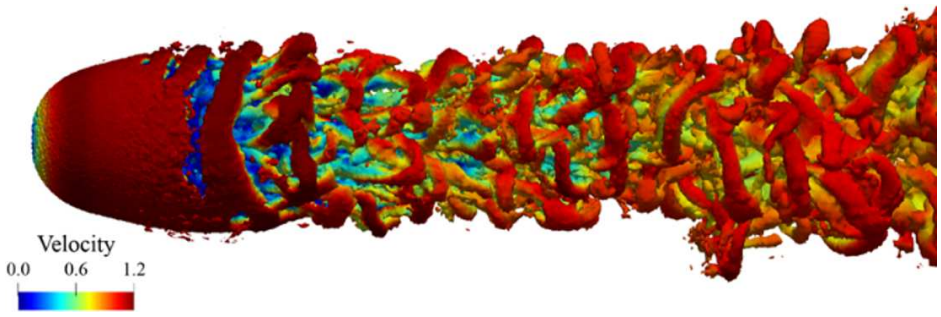

FIG. 12: Turbulent flow around immersed sphere at Reynold's number Re = 10,000

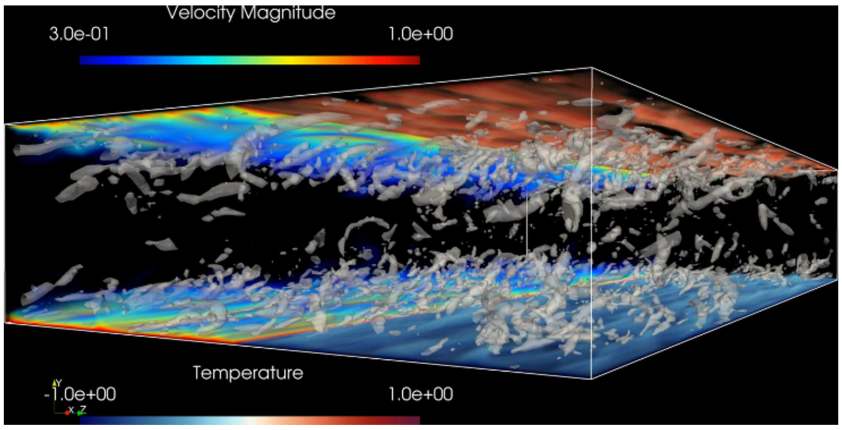

FIG. 13: Density stratified Plane Couette flow

in domain decomposition or substructure modeling, contact and friction in mechanical systems, and delamination at bimaterial interfaces in composites (Fig. 14).

The complexity engendered by mixed field problems increases the challenge of validating the numerical solution and quantifying uncertainty in these simulations. A significant attribute of the VMS and VMDG methods is that they come equipped with built-in error estimation module (Hauke and Garcia-Olivares, 2001; Hughes et al., 1998a; Masud and Truster, 2013; Masudr et al., 2012), which can help with verification and validation of the models and the method. The fundamental mathematical constructs in these works transcend the traditional fluid and solid/structural mechanics subdisciplines and therefore yield numerical methods with enhanced stability properties for application to coupled field problems in engineering and sciences.

5. A MULTIRESOLUTION WAVELET METHOD FOR MULTISCALE AND MULTIPHYSICS APPLICATIONS (C.H., L.D., K.M., AND D.L.)

Many useful computational science and engineering applications must solve PDEs with spatial and temporal scales across many orders of magnitude. For example, models of asteroid impacts (Boslough et al., 2015), supernova remnants (Malone et al., 2014), detonation combustion (Cai et al., 2016), the global ocean (Ringler et al., 2013), and the mechanics of materials (Matouš et al., 2017) are inherently multiphysics and multiscale. Various innovative numerical methods have been developed to address this computational challenge. For example, multigrid methods (Brandt, 1977; Yushu and Matouš, 2020), Chimera overset grids (Benek et al., 1989), remeshing/refining finite-element methods (FEM) (Gui and Babuška, 1986; Rajagopal and Sivakumar, 2007), and adaptive mesh refinement (AMR) (Berger and Oliger, 1984; Fatkullin and Hesthaven, 2001) have achieved a great deal in contemporary computational modeling. However in many of these algorithms it is desirable to know *a priori* where the spatial and temporal refinement will be required; otherwise they become computationally expensive. In this work we advocate a wavelet-based method, which is well suited for problems with dynamically adapting spatial and temporal scales.

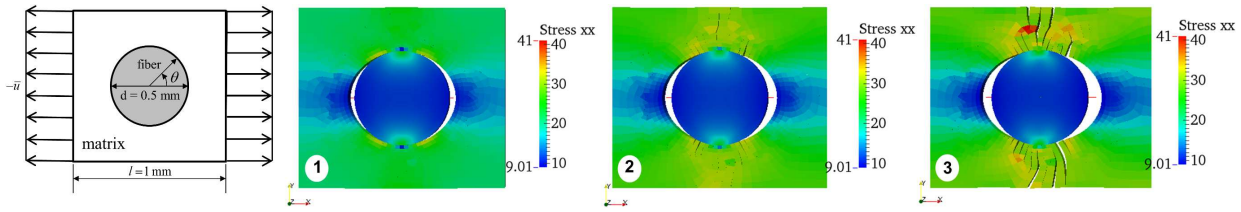

FIG. 14: Interfacial kinematic models, progressive interfacial failure, and the VMDG method

Wavelet-based numerical methods are particularly convenient for multiscale and multiphysics modeling because the multiresolution basis functions naturally provide adaptivity (Jawerth and Sweldens, 1994; Schneider and Vasilyev, 2010). To date, wavelet algorithms have been used in stochastic system modeling (Kong et al., 2016), multiscale model reduction (van Tuijl et al., 2019), solutions to coupled systems of nonlinear PDEs (Dubos and Kevlahan, 2013; Nejadmalayeri et al., 2015; Paolucci et al., 2014; Sakurai et al., 2017), bounded energy conservation (Qian and Weiss, 1993; Ueno et al., 2003), and significant data compression (Bertoluzza, 1996; Beylkin and Keiser, 1997; Liandrat and Tchamitchian, 1990). However, some implementations have had various restrictions, such as only solving PDEs with periodic or infinite domains (e.g., Fröhlich and Schneider, 1994; Goedecker, 1998; Iqbal and Jeoti, 2014), using computationally expensive dense grids (e.g., Le and Caracoglia, 2015; Lin and Zhou, 2001; Qian and Weiss, 1993), or requiring the use of finite difference operators for spatial derivatives, inhibiting the ability to solve PDEs in the wavelet domain and control accuracy of numerical differentiation (e.g., Holmström, 1999; Nejadmalayeri et al., 2015; Paolucci et al., 2014).

Therefore we have developed an algorithm designed to avoid the limitations of past wavelet methods while retaining their merits. Mathematical details regarding wavelet theory and the application of wavelets to the solution of PDEs can be found in Harnish et al. (2018, 2021). Here we describe a brief overview of our numerical method and demonstrate its capabilities on a multiscale and multiphysics example from Harnish et al. (2021).

5.1 Wavelet Theory and Numerical Implementation

Our algorithm is designed to solve initial boundary-value problems with error control on finite domains using a sparse multiresolution spatial discretization. In each application the initial conditions are projected onto the wavelet basis $\boldsymbol{\phi}^0_{\vec{k}}(\vec{x})$ and ${}^{\lambda}\boldsymbol{\psi}^j_{\vec{k}}(\vec{x})$, where $\vec{\bullet}$ indicates a vector. For example, the wavelet representation of a continuous function $f(\vec{x})$ in N spatial dimensions is given by

$$f_\varepsilon(\vec{x}) = \sum_{\vec{k}} s^0_{\vec{k}}\, \boldsymbol{\phi}^0_{\vec{k}}(\vec{x}) + \sum_{j=1}^{j_{\max}} \sum_{\lambda=1}^{2^N-1} \sum_{\{\vec{k}:|{}^{\lambda}d^j_{\vec{k}}|\geq\varepsilon\}} {}^{\lambda}d^j_{\vec{k}}\, {}^{\lambda}\boldsymbol{\psi}^j_{\vec{k}}(\vec{x}). \tag{4}$$

In Eq. (4), wavelet coefficients ${}^{\lambda}d^j_{\vec{k}}$ with magnitudes below a threshold ε are discarded along with their corresponding collocation points. Forward and backward wavelet operations are performed in our implementation using sparse, banded matrix operators. Additionally, the αth-order spatial derivatives in the i direction are applied directly to the continuous wavelet basis functions through the use of a matrix operator $\mathcal{D}^{(x_i,\alpha)}$. This process creates a sparse multiresolution spatial discretization where the spatial errors for fields and their derivatives are given by

$$\|f(\vec{x}) - f_\varepsilon(\vec{x})\|_\infty \leq \mathcal{O}(\varepsilon) \quad \text{and} \quad \left\| f^{(x_i,\alpha)}(\vec{x}) - \mathcal{D}^{(x_i,\alpha)} f_\varepsilon(\vec{x}) \right\|_\infty \leq \mathcal{O}\left(\varepsilon^{1-\alpha/p}\right), \tag{5}$$

where p is an even integer that defines the order of the basis functions. Derivations of the error estimates and details regarding the construction of the matrix operators can be found in Harnish et al. (2018).

After projecting fields and their derivatives onto the wavelet basis, the PDEs are transformed into ordinary differential equations (ODEs) in time. Next, an explicit, embedded, Runge–Kutta time integration scheme (Fehlberg, 1970) is used to convert the ODEs into algebraic equations. This procedure updates the solutions from the time step n to a trial time step $n+1^*$. Moreover, this update provides an estimate of the temporal error and adjusts the time-step size Δt such that the temporal error is of the same order as the spatial error [i.e., $\mathcal{O}(\varepsilon)$]. A predictor-corrector strategy is used to iteratively insert new collocation points into the sparse discretization during temporal integration to ensure that the spatial accuracy remains bounded at each time step. When the trial time step is accepted as the true time step, some wavelet coefficients are no longer needed to satisfy the error bounds and their collocation points are pruned from the sparse computational grid as it evolves with the solutions of the PDEs. This algorithm has been implemented in the Multiresolution Wavelet Toolkit (MRWT) written using modern C++ and is multithreaded using OpenMP. The data structures are designed to leverage temporal and spatial locality, and are trivially vectorizable for right-hand-side computations. The core matrix operators for wavelet transforms and spatial derivatives are stored mostly matrix-free, with stencil contractions that are trivially parallelizable and scale well.

5.2 Numerical Examples

Various examples verifying the implementation of the algorithm described in Sec. 5.1 have been published in Harnish et al. (2018, 2021). Here we demonstrate the multiscale and multiphysics capabilities utilizing the Taylor-Sedov blast-wave setup, where the energy pulse is deposited in a compressible fluid, leading to the development of a spherical shock wave. This example requires solving the coupled system of nonlinear PDEs given by the conservation of mass, momentum, and energy:

$$\frac{\partial \rho}{\partial t} = -\nabla \cdot (\rho \vec{v}), \tag{6}$$

$$\frac{\partial}{\partial t}(\rho \vec{v}) = -\nabla \cdot (\rho \vec{v} \otimes \vec{v} - \boldsymbol{\sigma}) + \rho \vec{b}, \tag{7}$$

$$\frac{\partial}{\partial t}(\rho \widetilde{e}) = -\nabla \cdot (\rho \widetilde{e} \vec{v} - \boldsymbol{\sigma} \vec{v} + \vec{q}) + \rho \vec{b} \cdot \vec{v} + \rho r, \tag{8}$$

where $\widetilde{e} = e + \vec{v} \cdot \vec{v}/2$. In Eqs. (6)–(8), we solve for the density ρ, velocity $\vec{v}$, and specific internal energy e. This system requires closure equations to describe the Cauchy stress tensor $\boldsymbol{\sigma}$, the specific internal energy e, and the heat flux $\vec{q}$. In this work the source terms are set to zero (i.e., $\vec{b} = \vec{0}$ and $r = 0$), we define the stress tensor with the Newtonian fluid constitutive equation, and assume a calorically perfect ideal gas with Fourier's law of heat conduction. Additionally, the material parameters are set according to the values in Table 2.

The initial condition is made continuous by way of a Gaussian profile for the initial pressure, with an overpressure peak of 2 MPa and a standard deviation of $1/(10\sqrt{2})$ m. The semidiscretized Eqs. (6)–(8) are integrated using the embedded $\mathcal{O}(\Delta t^4)$ and $\mathcal{O}(\Delta t^5)$ explicit Runge–Kutta method developed in Fehlberg (1970). The temporal discretization, Δt, is chosen adaptively to retain $\mathcal{O}(\varepsilon)$ accuracy. The boundary conditions are set to maintain the initial conditions, and the simulation is stopped before the developing shock wave interacts with the computational boundary. Figure 15 shows the numerical solutions to Eqs. (6)–(8) at time $t = 133.902$ µs, generated with wavelet parameters $p = 8$ and $\varepsilon = 10^{-2}$.

For the numerical solution in Fig. 15, the MRWT discretization of the initial condition required only two resolution levels (i.e., $j_{\max} = 2$), which resulted in 31.250 mm between the closest collocation points at time $t = 0$. As the internal energy converted into kinetic energy, MRWT automatically refined the grid near regions of the developing shock wave. As shown in Fig. 15(a), MRWT predicted nine resolution levels (i.e., $j_{\max} = 9$) at time $t = 133.902$ µs, which resulted in 0.244 mm between the closest collocation points. A dense discretization at this length scale would require over 67 million collocation points, whereas the MRWT solution in Fig. 15 only contains 312,793 collocation points, resulting in a compression ratio greater than 200. Moreover, the sparse multiresolution spatial discretization maintains symmetry and adapts to follow features as they evolve through the domain.

5.3 Conclusions

When computational science and engineering applications contain dynamic fine-scale features, our proposed wavelet-based algorithm offers a significant improvement over traditional numerical methods. In particular, our approach is well suited for models which require dynamically adaptive resolution across multiple spatial and temporal scales. This is accomplished in our method by leveraging the properties of wavelet basis functions to automatically adapt the computational domain as needed to accurately resolve features. This work highlights the state of wavelet-based

TABLE 2: Material parameters for dry air at room temperature

Variable	Name	Value
γ	Ratio of specific heats	$7/5$
μ	Dynamic viscosity	1.9×10^{-5} Pa s
κ	Thermal conductivity	2.55×10^{-2} W/(m K)
c_v	Constant volume specific heat	7.18×10^{2} J/(kg K)

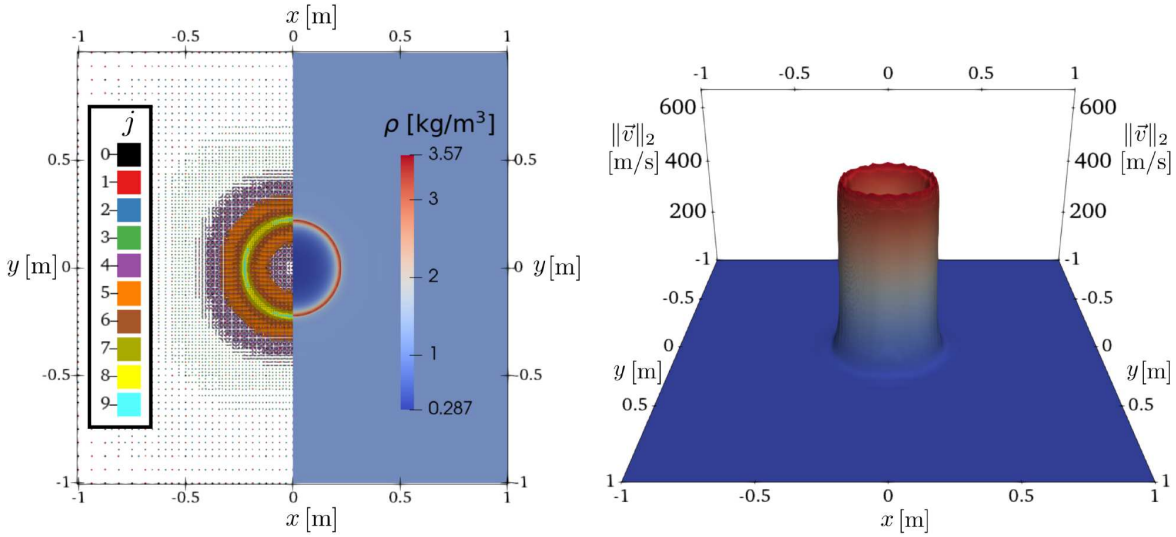

(a) (b)

FIG. 15: Sparse multiresolution grid and numerical solution at $t = 133.902$ µs obtained using $p = 8$ and $\varepsilon = 10^{-2}$. (a) MRWT solution of the density field ρ. The grid points are colored according to their resolution level j. (b) MRWT solution of the velocity field $\|\vec{v}\|_2$. The maximum velocity is approximately 568 m/s. The reader is referred to the online version of this article for clarity regarding the color in this figure. Results are taken from Harnish et al. (2021).

algorithms that evaluate spatial derivatives directly on the wavelet basis functions and ensures that the error is bounded at each time step. Furthermore, we demonstrate that MRWT is capable of multiscale and multiphysics modeling using compressed data on sparse multiresolution discretizations in finite domains.

6. PARAMETRICALLY HOMOGENIZED CONSTITUTIVE MODELS FOR MULTISCALE MODELING OF DEFORMATION AND CRACK NUCLEATION IN TITANIUM ALLOYS (S.G. AND S.K.)

Parametrically homogenized constitutive models or (PHCMs) have been recently developed for multiscale modeling of deformation and fatigue crack initiation in polycrystalline metallics alloys (Kotha et al., 2019a,b, 2020a,b; Ozturk et al., 2019a,b, 2021). PHCMs are thermodynamically consistent, macroscopic constitutive models that bridge spatial scales through the explicit representation of microstructural descriptors in equations that constitute these models. Coefficients in PHCM equations are explicit functions of representative aggregated microstructural parameters or (RAMPs), representing statistical distributions of morphological and crystallographic descriptors of the microstructure. Their distinct features offer them the following advantages:

- Explicit representation of microstructural descriptors, specifically RAMPs, in macroscopic constitutive relations is an attribute with important implications in structure-material design.
- Very high efficiency with good accuracy of multiscale solutions is a requirement for most data-driven design algorithms.

The physics-based PHCM formulations for finite deformation plasticity developed in Kotha et al. (2019a,b, 2020a,b) and Ozturk et al. (2019a,b, 2021) have a consistent thermodynamic framework for dissipative, irreversible processes. Following the second law of thermodynamics, general forms of equations representing the evolution of state variables in PHCMs are *a priori* selected to reflect the fundamental deformation characteristics of the material including objectivity, rate dependence, anisotropy, tension-compression asymmetry, history/path dependence, Bauschinger effect, etc. The PHCM equations are chosen to be consistent with the aggregated response of micromechanical crystal plasticity finite-element-model (CPFEM) simulations of microstructural statistically equivalent

representative volume elements or (M-SERVEs) (Bagri et al., 2018). The first law of thermodynamics, governing the mathematical theory of homogenization through energy equivalence, bridges length scales and expresses constitutive coefficients as functions of RAMPs, e.g., in the form of texture tensor, grain size and orientation distribution, lattice descriptors, etc.

This section focuses on the application of the PHCMs for modeling deformation and fatigue crack nucleation in Ti alloys such as Ti64 and Ti6242. These materials are widely used in aerospace applications such as in turbine engine disks and aircraft panels. The microstructures of these alloys are characterized by a high degree of heterogeneity in the form of grain structures with significant anisotropy as well as tension-compression asymmetry. The mechanical response and crack nucleation in these alloys have been found to be strongly influenced by local microstructure (Ozturk et al., 2017). Phenomenological models, typically employed for structural analysis, ignore microstructural influence, while pure micromechanical analysis using the crystal plasticity finite element (CPFE) method incurs huge computational cost. To conduct structural simulations, accounting for the microstructure, the computationally efficient PHCM and a parametrically homogenized crack nucleation model (PHCNM) (Kotha et al., 2019a,b, 2020b; Ozturk et al., 2019a,b, 2021) are used. Multiscale validations have also been conducted for uniaxial and biaxial cruciform tensile experiments in Maloth et al. (2020).

6.1 Developing the Parametrically Homogenized Constitutive Model (PHCM)

The steps in the development of the PHCMs are delineated in Table 3. Module I represents the acquisition of microstructural and mechanical test data for calibration and validation of the CPFEM and PHCMs. In module II, microstructure-based, statistically equivalent RVEs or M-SERVEs are first established. Following this, size-, rate-, and temperature-dependent image-based CPFEM is used to perform detailed micromechanical simulations of the M-SERVEs. Module III begins with the creation of a database of evolving variables from CPFEM simulations of the M-SERVEs with various microstructural and loading combinations. The RAMPs of morphological and crystallographic descriptors, such as grain size, shape, orientation, and misorientation distributions, are subsequently identified from detailed sensitivity analysis, e.g., Sobol analysis. In module IV, functional forms of PHCM constitutive coefficients, e.g., elastic stiffness coefficients, anisotropic yield function coefficients, and hardening moduli, are expressed as functions of RAMPs using machine-learning tools, operating on a database of constitutive coefficients obtained from CPFEM simulations of the M-SERVEs. These constitutive parameters also incorporate state variables representing the upscaled effect of microstructural deformation mechanisms. The PHCMs are readily incorporated in commercial FE software like ABAQUS through user-defined material modeling interfaces such as UMAT for microstructure-sensitive structural response predictions. Finally, uncertainty quantification is built into the PHCM framework following a Bayesian inference formulation (Kotha et al., 2020a,b; Ozturk et al., 2021) to derive probabilistic microstructure-dependent constitutive laws of the macroscopic response. A significantly reduced number of solution variables in the PHCM simulations, compared to direct numerical simulations (DNS) of micromechanical models, make them several orders of magnitude more efficient with good accuracy.

6.2 Parametrically Homogenized Crack Nucleation Model (PHCNM)

Grain-level crack nucleation in Ti alloys has been observed to occur at grain boundaries between a soft grain (favorably oriented for plastic slip) and a hard grain (unfavorably oriented for plastic slip) (Anahid et al., 2011; Ozturk et al., 2017) under certain load conditions. During the load hold period of a dwell fatigue problem, the soft grain undergoes time-dependent plastic deformation, leading to dislocation pileups in the soft grain boundary and subsequent stress concentration at the adjoining hard grain boundary that deforms elastically. From these physical observations, a grain-level, probabilistic crack nucleation criterion has been proposed in Anahid et al. (2011) and Ozturk et al. (2017), with the assumption that a wedge crack nucleates into the hard grain as a consequence of the closure failure of the Burgers circuit surrounding piled-up dislocations in the neighboring soft grain. This model has been calibrated and validated with crack nucleation experiments. The PHCNM corresponds to a macroscopic signature of fatigue crack nucleation in grains of the underlying microstructure. Analogous to the process of developing PHCMs, the PHCNMs are generated from a database of the grain-scale probabilistic crack nucleation simulations. The probability of crack nucleation

TABLE 3: Steps in the development of the parametrically homogenized constitutive models (PHCMs) with uncertainty quantification

Module I: Experimental Data Acquisition	**Module II: Image-based Micromechanical Models**	**Module III: Sensitivity for Identifying RAMPs**	**Module IV: PHCM Calibration-Validation**
Generate EBSD data from experimental microstructures	Generate microstructure-based SERVEs (M-SERVEs)	Generate virtual microstructures from a range of parameters	Generate training data from CPFE analysis of various SERVEs and loading conditions
Conduct mechanical tests for deformation and crack nucleation	Calibrate crystal plasticity and crack nucleation model	Identify critical micro-distributions and corresponding RAMPs	Identify functional forms of RAMPs in PHCM coefficients by **machine learning**
Generate statistical distributions of descriptors in the microstructure	Validate image-based CPFE model with experimental data	Establish RAMPs for PHCM coefficients using Sobol analysis	Implement in macroscopic FE codes and validate structural applications
			Incorporate uncertainty quantification/ propagation

in PHCNMs is obtained at the macroscale as a function of macroscopic mechanical variables such as stresses, plastic strain, and also the underlying RAMPs of the microstructure. The PHCNM has been validated against coupon-level experiments under dwell loading conditions in Ozturk et al. (2019a,b).

6.3 Determining the Multiscale Response of Turbine Engine Blade using PHCM and PHCNM

The effect of microstructure on mechanical response and crack nucleation probability of a prototype turbine engine blade is studied using PHCM- and PHCNM-based structural simulations. The turbine engine disk is shown in Fig. 16. An angular segment of the disk simulated in ABAQUS is shown in Fig. 16(b). The finite-element model of the blade consists of 147,136 number of 10 noded tetrahedral elements. The two opposite faces of the hub are constrained with roller supports to maintain axial symmetry. All the nodes in the model are subjected to centrifugal loading corresponding to an angular velocity (ω) of 7200 rpm for a total of 170 h. This loading corresponds to approximately 5000 take-off operations, each lasting 2 minutes, and models the operating conditions of the disk (Ozturk et al., 2021).

Two different simulations corresponding to extruded microstructures of the Ti alloy Ti64 are illustrated in Figs. 17(a) and 17(b). These two microstructures have a similar average grain size of ($\sim$ 19 μm), but their crystallographic orientations differ as shown in their pole images. The RAMPs corresponding to these two microstructures are calculated and assigned to all the elements in the model for PHCM simulations. Each ABAQUS simulation takes approximately 2 CPU hours with 24 cores, with only a fraction of the total time actually spent in PHCM and PHCNM simulations.

The mechanical response and crack nucleation probability along the rim of the blade [AB in Fig. 16(c)] are studied to understand the influence of microstructure. The mechanical response variables, such as maximum tensile principal stress ($\sigma_{(max,prin)}$) and the effective plastic strain ($\bar{\epsilon}_{\mathrm{p}}$), which are important for nucleating the crack, are plotted in Fig. 18(a) at one of the critical locations C along the path AB. The material locally undergoes stress relaxation while accumulating plastic strain. The microstructure MS2 accumulates more plastic strain as compared to MS1, which may be attributed to the larger volume fraction of grains favorably oriented for plastic slip in MS2. The

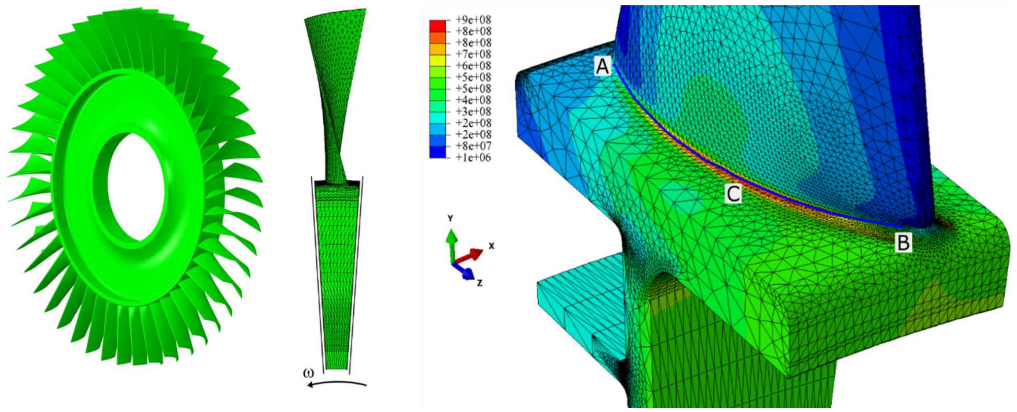

(a) (b) (c)

FIG. 16: Turbine engine disk: (a) prototype engine disk, (b) angular segment of the disk blade simulated in ABAQUS, and (c) von Mises stress contours at the end of the simulation using microstructure MS1

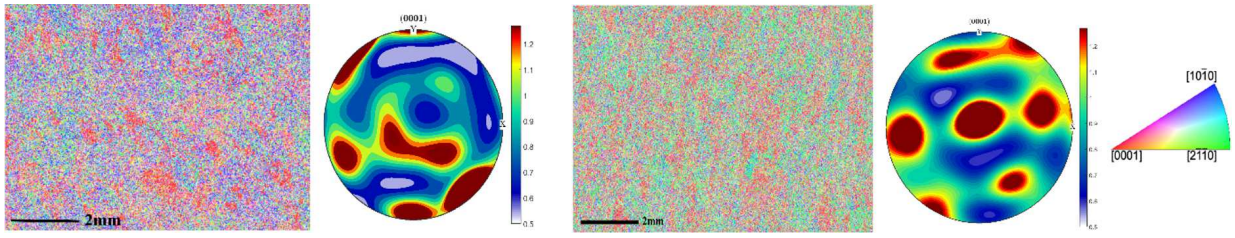

(a) (b)

FIG. 17: Extruded microstructure simulations. Inverse pole figure maps and pole figures of the electron back-scattered diffraction (EBSD) images of two extruded microstructures. (a) MS1. (b) MS2 showing crystallographic orientations.

maximum crack nucleation probability (P_{nucl}) in the model has been observed at point C in both simulations, and its time history is plotted in Fig. 18(a). As a result of higher plastic strain accumulation and the underlying RAMPs, the microstructure MS2 undergoes earlier crack nucleation ($P_{\text{nucl}} = 0.95$) as compared to MS1 under the same loading conditions. This study illustrates how PHCM and PHCNM simulations give more insights into the microstructural influence and thus may be used in subsequent material design.

These material microstructure-integrated constitutive models are invaluable for predicting the structural response of Ti alloys, viz. Ti64. The PHCMs are superior to many of the homogenization-based multiscale models in terms of efficiency and their application to real structural problems. The constitutive parameters in PHCMs have an explicit dependency on the representative aggregated microstructural parameters or RAMPs, which provide a connection between the structural response and microstructure. Incorporation of uncertainty quantification in the UQ-PHCM formulation using Bayesian inference has been pursued by Kotha et al. (2020a,b) and Ozturk et al. (2021) to quantify the uncertainty in constitutive parameters, and a Taylor-expansion-based uncertainty-propagation method is used to propagate the uncertainty to mechanical response variables.

7. MULTISCALE MODELING FOR DYNAMICS OF ARCHITECTED MATERIALS AND STRUCTURES (C.O.)

Architected materials constitute a unique class of materials that exhibit mechanical and functional properties that are not observed in natural materials or traditional composites. This class of materials originates from building

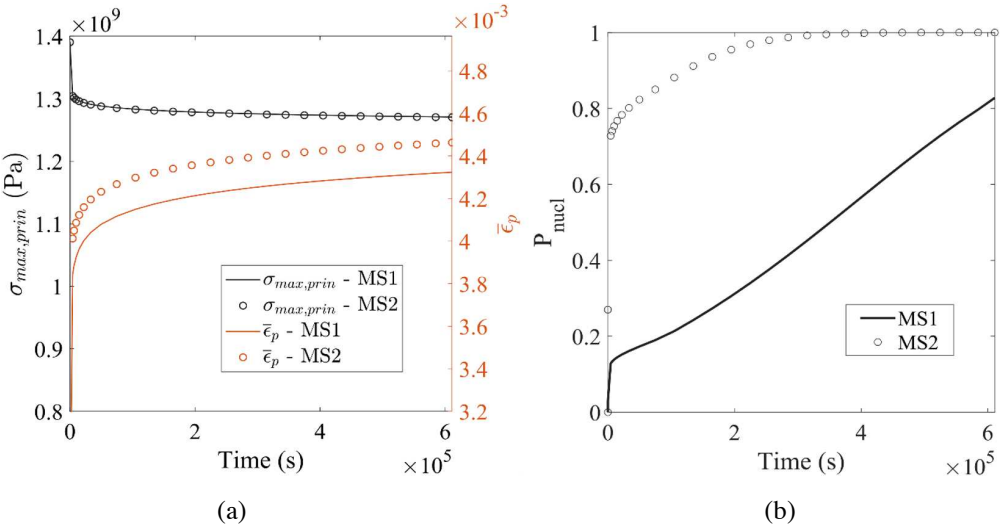

FIG. 18: Time history of (a) maximum tensile principal stress, effective plastic strain, and (b) nucleation probability at a critical point C in Fig. 16(c)

complex microstructures (lattices, shellular structures, continua) made of different discrete or continuous building blocks and/or multiple materials. The advent of additive manufacturing is a major facilitator of architected materials, where microstructures are either too costly or complex to construct using subtractive processes. These unique properties do not only improve the performance of existing engineering applications but also bring to bear completely new engineering concepts that are otherwise not possible. Such novel applications include but are not limited to elastic cloaking (Stenger, 2012), acoustic superlens (Kaina et al., 2015), topological insulators (Mousavi et al., 2015), and waveguides (Khelif et al., 2004), among others. A tremendous number of architected material concepts are being investigated for static (i.e., mechanical metamaterials) as well as dynamic conditions at a wide range of frequencies (e.g., acoustic and optical metamaterials). Particularly in the context of wave propagation applications, multiscale modeling and simulation of the dynamic response of architected materials such as phononic crystals and acoustic metamaterials presents many opportunities and significant challenges due to the scale- and size-dependent interactions between waves and the material microstructure. Because of this reason, there has been significant recent research activity in this domain. In this section we focus on some of the recent developments in multiscale modeling of phononic crystals and acoustic metamaterials for the purpose of controlling mechanical and acoustic waves.

Several new computational approaches have been recently proposed to describe the transient dynamic behavior of architected materials and probe the topological and material property spaces in search of a better understanding of the structure-dynamic property relationships. These approaches include but are not limited to computational homogenization (Liu and Reina, 2019; Roca et al., 2018; Sridhar et al., 2016), homogenization methods based on Willis' theory (Meng and Guzina, 2018; Nassar et al., 2016; Sridhar et al., 2018), the multiscale finite element method (Casadei et al., 2016), and the method of computational continua (Filonova et al., 2016), among others. Some of these methodologies operate at the scale separation limit, where the microstructure size is much smaller compared to the deformation wavelength. These methodologies are particularly suited for locally resonant materials typically generated by relative deformation within the microstructure facilitated by large density mismatch between the material constituents. Wave propagation in phononic crystals are affected by Bragg scattering at the short-wavelength regime. When the deformation wavelength approaches the size of microstructure, the assumption of scale separation is no longer valid, and methodologies that do not rely on the scale separation assumption are needed to capture the transient dynamic response patterns.

An alternative approach to modeling behavior when the lengths of the propagating waves are near (but longer than) the characteristic size of the material microstructure is asymptotic homogenization with high-order expansions. While the inclusion of first-order asymptotics result in the classical homogenization models for the long-wavelength

response, the inclusion of high-order asymptotics results in nonlocal macroscale governing equations. In this approach the length-scale parameters associated with the high-order terms are typically directly obtained from the material microstructure through homogenization operations. Early pioneering work by Fish et al. (2002a,b) on asymptotic homogenization for transient dynamics focused on characterization of dispersion in composite materials. More recently, this approach has been extended to predict the attenuation and dispersion of transient waves in architected materials made of elastic and viscoelastic constituents (Hu and Oskay, 2017, 2019; Hui and Oskay, 2013, 2014, 2015). A critical step toward achieving asymptotic homogenization models that can capture the dynamic response patterns including attenuation and dispersion is the incorporation of appropriate spatiotemporal terms in the construction of the nonlocal models.

Figure 19 illustrates the capabilities of high-order asymptotic homogenization modeling in capturing the complex wave propagation behavior in a composite material (Hu and Oskay, 2018). The simulations compare the predictive capability of a spatiotemporal nonlocal multiscale model and the direct numerical simulations performed using the finite-element method on the macroscopic domain by fully resolving the material heterogeneity. The macroscopic domain is made of a square unit cell with two material constituents (i.e., matrix and elastic circular inclusion). Two cases are considered where the matrix is taken to respond elastically and viscoelastically under the applied loading. The loading is imparted on the domain such that the predominant propagating wave is in antiplane shear mode. The figure compares the propagating waves at two time instances as predicted by the direct numerical simulation and the asymptotic homogenization method. In the case of a viscoelastic matrix, wave propagation at the imparted velocity results in a strong interaction between material damping and dispersion induced by the heterogeneity that results in achieving significant wave attenuation. When the applied frequency is within the stop band of the material (not shown in the figure), the traveling shear wave completely attenuates in both elastic and viscoelastic cases, demonstrating the efficacy of the approach even beyond the dispersion regime.

More recently, the variational multiscale enrichment (VME) approach has been proposed to model the transient dynamic response of architected materials (Hu and Oskay, 2020). A key distinguishing factor between VME and the aforementioned homogenization methods is that the former does not employ the principle of scale separation. This allows the VME approach to be effective in modeling both Bragg scattering and local resonance excited at a broad spectrum of frequencies, providing a unified framework for architected materials. Compared to the high-order asymptotic methods, the structure as well as the formulation of VME is significantly simpler, potentially offering wider applicability for problems that involve more complex phenomena and nonlinear material behavior. VME is based on the additive decomposition of the displacement field into coarse and fine-scale counterparts in the variational form and

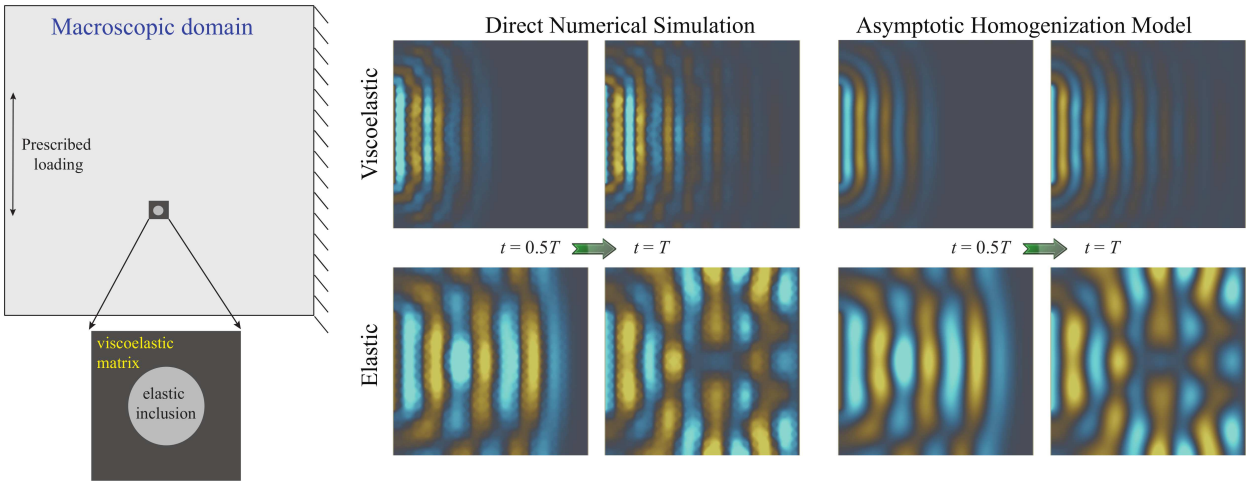

FIG. 19: Wave propagation in viscoelastic and elastic composites as predicted by direct numerical simulation and the asymptotic homogenization models demonstrating the combined attenuating effects of Bragg scattering and viscous damping. The data associated with these results are initially published in Hu and Oskay (2018).

effective numerical evaluation of fine- as well as the coarse-scale fields. Numerical evaluation of the fine-scale fields in VME is in contrast with the classical variational multiscale method (Hughes et al., 1998b) that typically employs analytical functions to approximate the fine-scale response and is more similar to the numerical subgrid upscaling approach (Arbogast, 2002). When modeling the transient dynamic response, short waves must be characterized accurately on the coarse grid, where the element size could exceed the wavelength. In order to ensure accuracy, high-order spectral elements are therefore utilized. The computational efficiency of the multiscale approach is achieved by considering reduced-order modeling (ROM) at the fine scale. The ROM approach relies on a material-phase-based mode synthesis (Craig and Bampton, 1968) and characteristic constraint mode reduction (Castanier et al., 2001).

Figure 20 shows the verification of the spectral variational multiscale enrichment method in the context of an elastic waveguide problem (Hu and Oskay, 2020). The simulations compare the predictive capability of the multiscale model with the direct numerical simulations. The domain of the waveguide is a periodic arrangement of a phononic crystal unit cell, with the exception of an elbow-shaped path made of homogeneous material. The macroscopic domain is subjected to harmonic compression-tension loading. The figure shows the lateral component of the velocity as predicted by the multiscale and direct numerical simulations. The frequency of the imparted wave lies within the stop band of the phononic crystal. The wave therefore is not expected to propagate through the phononic crystal but is permitted to propagate unimpeded within the homogeneous region of the domain. As the wave enters the vertical part of the homogeneous path, the wave turns and propagates vertically, whereas the lateral propagation is once more prohibited via Bragg scattering. A similar change of direction occurs at the second junction of the elbow. This process was accurately modeled using both the direct numerical simulations as well as the multiscale approach. A key benefit of the multiscale methodology is that the computational cost is over one order of magnitude lower for the multiscale approach. The elbow-shaped elastic waveguide was previously investigated experimentally using a periodic array of steel cylinders in water (Khelif et al., 2004).

8. MULTISCALING FOR REINFORCED CONCRETE STRUCTURES (J.F. AND A.M.)

With an annual production of more than 23 billion tons, concrete is the most used material in the construction industry worldwide (Miller et al., 2018). Since the environmental impact of concrete is considerable due to CO_2 emissions, water consumption, and the landscape for aggregate mining, just to name a few, efficient design of reinforced concrete structures is of the utmost importance to the society.

Since the early 1900s, there have been considerable research efforts aimed at developing theories and methods to predict its behavior. The first code published in North America with specific recommendations for the analysis and design of reinforced concrete was published in 1910 by the American Concrete Institute (ACI), which now publishes the Building Code Requirements for Structural Concrete with its latest edition published in the 2014 American Concrete Institute Committee 318 (2014). Practitioners have long realized that stiffness and strength of concrete structures must reflect, among other things, cracking, plasticity, creep, and shrinkage; this has been done in the form

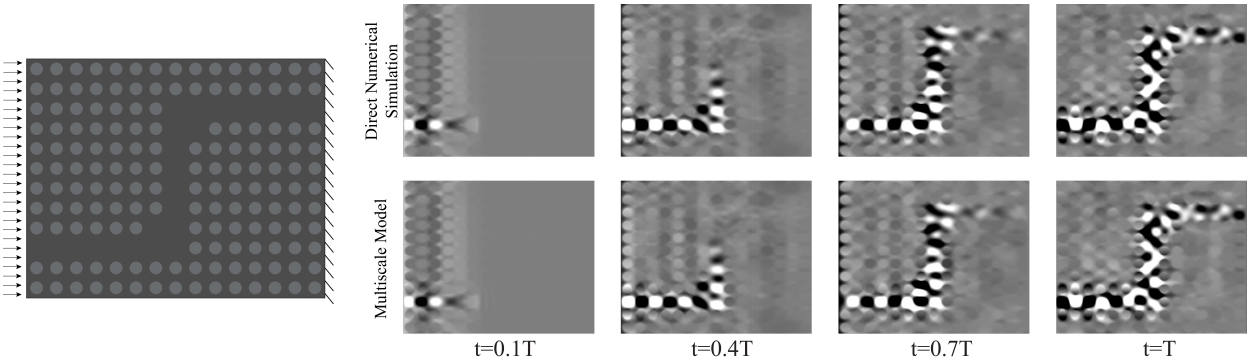

FIG. 20: Wave propagation in an elastic waveguide predicted by the spectral variational multiscale approach at a fraction of the direct numerical simulation. The results are reprinted from Hu and Oskay (2020).

of semiempirical reduction factors and recommendations that are still used in codes today. Research efforts aimed at detailed numerical analysis of concrete structures span more than 40 years. Material models developed in recent years employ a combination of damage mechanics and plasticity.

Prior to the year 2000, the literature on multiscale methods for reinforced concrete has been rather limited, but interest in multiscale methods accelerated over the past two decades, as can be seen from Fig. 21. One of the major hurdles in utilization of multiscale methods for large-scale concrete structures is their computational complexity. This is because modeling each beam, column or slab with multiple continuum elements is computationally not feasible. Furthermore, resolving three-dimensional microstructural features of reinforced concrete for nonlinear problems where a discretized RVE problem has to be repeatedly solved is not computationally feasible either. The primary objective of this section is to describe an application of the most recent multiscale approaches developed for the reinforced concrete structures. For the mathematical theory, we refer to the references included herein.

8.1 Higher Order Computational Continua (HC^2)

A higher-order computational continua (HC^2) formulation developed for the analysis of reinforced concrete beams (Moyeda and Fish, 2018a,b) and solid, waffle, and hollowcore reinforced concrete slabs (Moyeda and Fish, 2019) has been gaining traction among structural designers. The salient features of the (HC^2) formulation are (i) the ability to consider large RVE characteristic to waffle and hollowcore slabs, (ii) versatility stemming from the ease of handling damage, prestressing, creep, and shrinkage, and (iii) computational efficiency resulting from model reduction, combined with the well-established damage law rescaling method that yields simulation results nearly mesh-size independent. The multiscale formulation has been validated against experimental data for solid, hollowcore, and waffle-reinforced concrete slabs, with and without prestressing.

The classical O(1) homogenization approach assumes constant coarse-scale strain over the RVE domain, which holds true when the size of the RVE is small compared to the macroscopic element. For problems involving bending of reinforced concrete elements, the macroscopic strain varies not only through the thickness, but may also vary in between the stirrup, which comprises the three-dimensional domain of the RVE in the HC^2 approach. Figure 22 schematically depicts the homogenization procedure based on the variation of the macroscopic strain.

The HC^2 formulation has been applied for the design of the reinforced concrete pier depicted in Fig. 23 that supports the elevated railway for line 3 of the metro system in Monterrey, México. The displacement of a pier is of critical importance, as it affects the comfort of the metro riders.

The pier cap is modeled as a simple supported beam with a span of 16.0 m; its cross section and RVE partitions are shown in Fig. 24(a). The cap uses 32 longitudinal reinforcement bars 32 mm in diameter with yield stress of 420 MPa and four post-tension cables, each cable comprised of 16 prestressing strands 15 mm in diameter with an ultimate strength of 1860 MPa. Reinforcements against shear failure are vertical stirrups 20 mm in diameter spaced

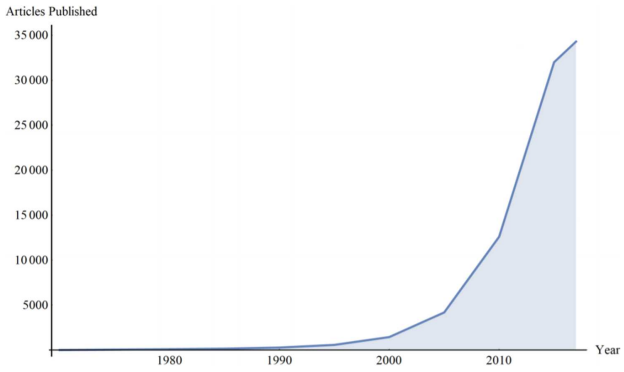

FIG. 21: Number of articles published with the phrase "Multiscale Concrete" in the text per Google Scholar (2018)

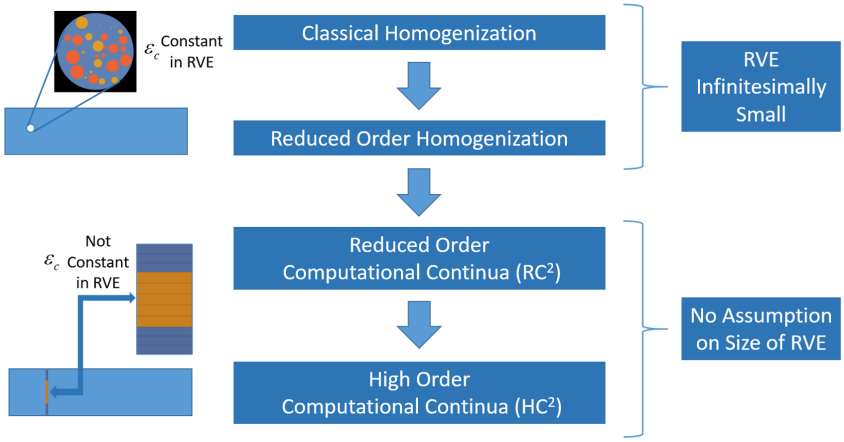

FIG. 22: Elevation of the pier for the elevated railway in Monterrey, México. The loads represent the bearings of the superstructure beam.

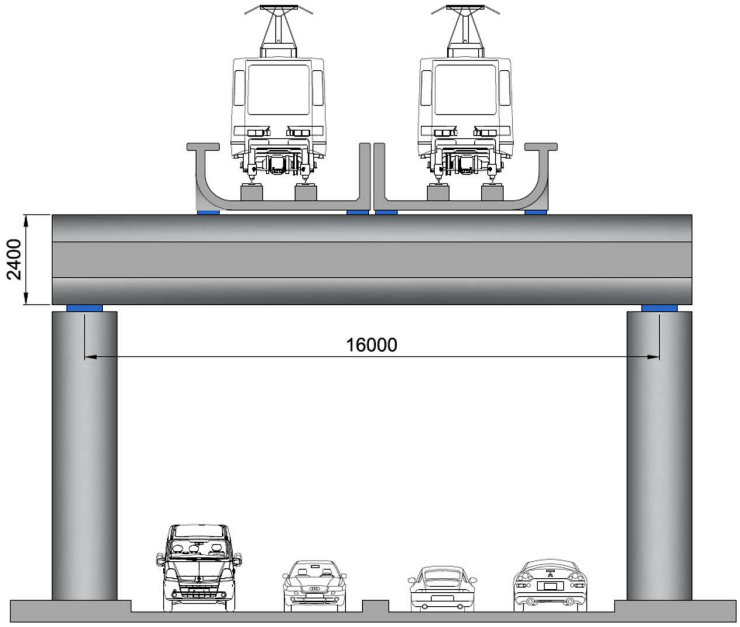

FIG. 23: Reduced-order methods for infinitesimal (top) and arbitrary size (bottom) representative volume elements (RVE)

at 150 mm in six vertical legs. The reinforcement mesh in the RVE is shown in Fig. 24(b). The concrete for the pier has a compressive strength of 35 MPa and modulus of elasticity of 27,710 MPa.

The results of the nonlinear analysis are shown in Fig. 25, where the corresponding load versus displacement is obtained and compared to the design requirements. From the analysis, it is clear that the pier cap is capable of resisting acting loads on the structure. The displacement from the live load and impact is less than L/1600 and is therefore adequate.

8.2 Sliced Statistical Reduced-Order Homogenization

A short-steel-fiber–reinforced ultrahigh-performance concrete known as Cor-Tuf is widely employed as a building material due to its exceptional mechanical behavior. Cor-Tuf exhibits high compressive strength in addition to high

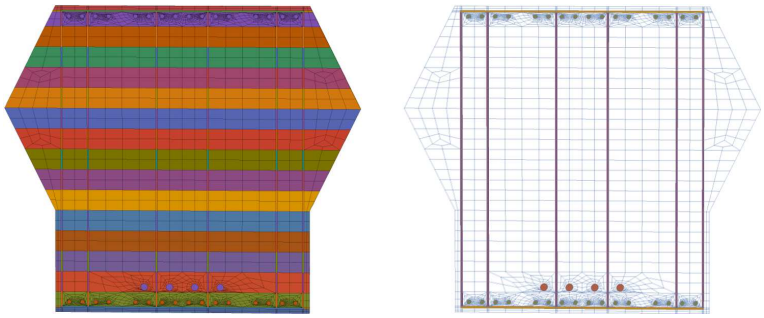

(a) (b)

FIG. 24: Pier cap. (a) Finite-element mesh of the RVE and its partitions shown in colors. (b) Finite-element mesh of the reinforcement, prestressing, and stirrups.

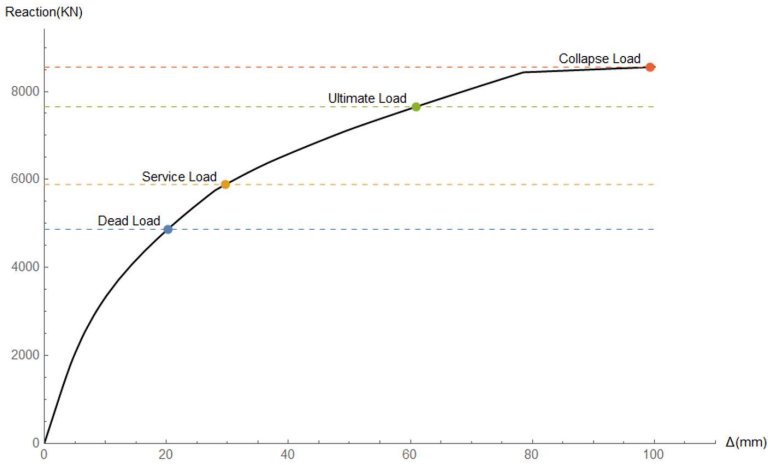

FIG. 25: Load versus displacement curve for the pier cap and its corresponding design loads

tensile strength stemming from the steel reinforcement (Pajak and Ponikiewski, 2013). The main challenge is in predicting strength and postfailure behavior of the Cor-Tuf material under general loading conditions. As an illustration, consider a fiber-reinforced concrete (Trainor et al., 2013) scanned using an X-ray computed tomography (CT) imaging system that permits characterization of its internal features. Based on the unsupervised separation and classification of merged objects in three dimensions (Tal and Fish, 2018), a database of location and alignment of all fibers is depicted in Fig. 26(a). Figures 26(b)–26(d) depict groups of fibers closely aligned with a certain angle.

The sliced statistical reduced-order homogenization model (ROH) (Huang et al., 2019) for short-fiber–reinforced composite consists of slices of short-fiber unit cells depicted in Fig. 27. The Voight approximation (Voigt, 1889) (or so-called Taylor's kinematical assumption) is employed by which the fine-scale strain in each slice is assumed to coincide with that on the macroscale. The orientation of the fiber in each slice is defined to represent statistical distribution of fibers. Numerical experiments suggest that the optimal number of slices is 7, which is a default parameter in Multiscale Designer Win.

The sliced statistical ROH model has been applied for analysis of the Malukou composite girder cable-stayed bridge in Hunan Province of China, spanning nearly 1 km. The composite girder is composed of a 170-mm-thick ultrahigh-performance fiber-reinforced concrete (UHPFRC) deck slab reinforced with 18- and 12-mm steel bars, in longitudinal and transverse directions, respectively, both spaced at 70-mm intervals. A comparative study by Wang et al. (2020) has been performed for the four-point bending test problem shown in Fig. 28.

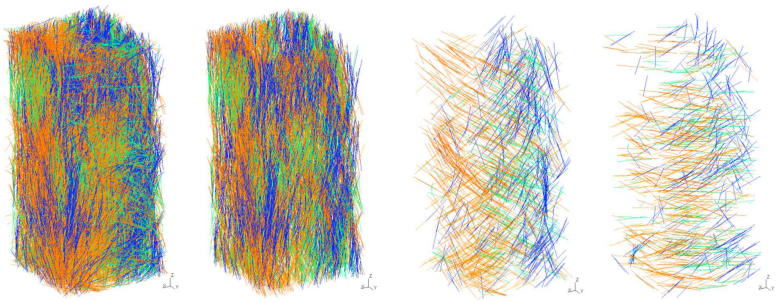

(a) (b) (c) (d)

FIG. 26: Distribution of location and alignment of short steel fibers: (a) all fibers, (b) $\theta \in [0, \pi/12]$, (c) $\theta \in [\pi/6, \pi/4]$, and (d) $\theta \in [\pi/3, \pi/12]$

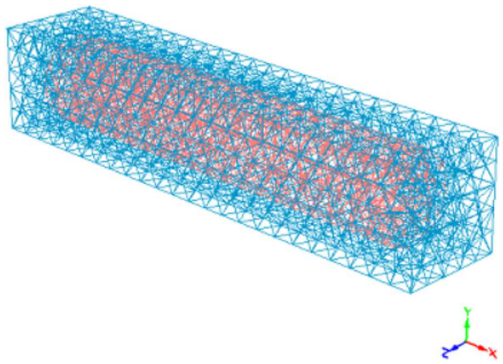

FIG. 27: Finite-element unit cell of a single discontinuous fiber slice

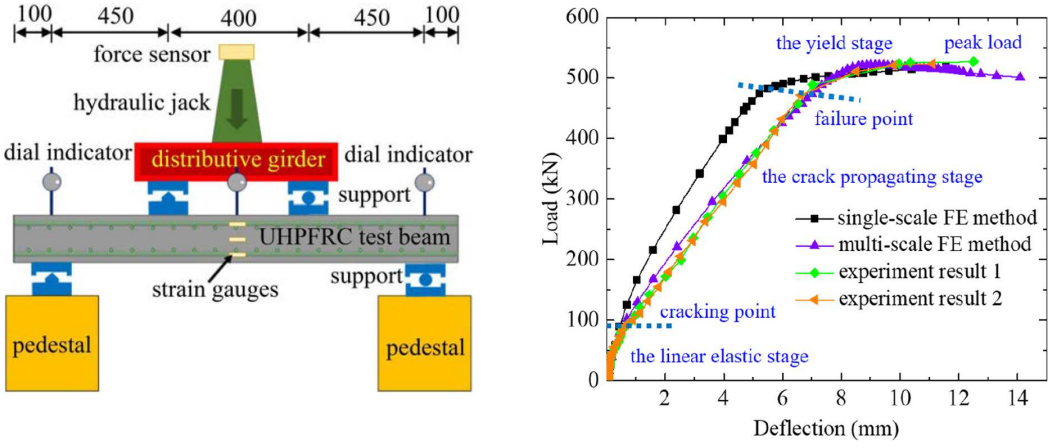

(a) (b)

FIG. 28: Four-point bending test: (a) model schematics (units: mm) and (b) comparison of single-scale, sliced statistical ROH (multiscale) and experimental results

8.3 Future Outlook

One of the most promising directions that may further propel the field of multiscale science and engineering and accelerate adoption of multiscale technologies for reinforced concrete structures appears to be the harnessing of

machine-learning and other artificial intelligence (AI) approaches for linking scales (Fish et al., 2021). The distillation of numerous fine-scale simulations, each involving extremely large numbers of degrees of freedom, into models describing overall behavior of large-scale reinforced concrete structures seems to be a natural task for such data-driven methods. Often overlooked is the role that AI may have in the reverse process: the initialization of fine-scale configurations, consistent with a given coarse-scale state, that represent a realistic ensemble and whose simulation can be used to determine the mean behavior. The development of computational methods that combine physical principles (such as conservation of mass, momentum, and energy) with data-driven constitutive models is a burgeoning topic in the field of computational science (Kirchdoerfer and Ortiz, 2016).

9. SUMMARY

From biology to engineering, multiscaling is necessary and successful at bridging and connecting disparate spatial and temporal scales to make possible concrete applications. We now have excellent tools for modeling the large biological molecules of life, including our genome and viruses, and various materials in industry and the human body, from bridges, airplanes, to human bones, and we can visualize and simulate motions in our oceans and galaxies. Such applications are invaluable for medicine, technology, and industry, and will only increase in importance. As computer hardware advances, with contributions from cloud computing, quantum computing, and neuromorphic networks, our software and modeling innovations will require new developments as well. With greater anticipated participation of knowledge-based information, such as machine-learning tools, modeling and simulation have a bright future as never before.

ACKNOWLEDGMENTS

T.S. gratefully acknowledges funding from the National Science Foundation through RAPID Award No. 2030377 from the Divisions of Mathematical Sciences and of Chemistry, National Institutes of Health, R35GM122562 Award from the National Institute of General Medical Sciences, and Philip-Morris International. C.O. gratefully acknowledges funding from the National Science Foundation CMMI MOMS and CDS&E programs (Grant No. 1435115). C.H., L.D., K.M., and D.L. gratefully acknowledge Los Alamos National Laboratory (LANL) for Awards No. 369229 and No. 370985.

AUTHOR CONTRIBUTIONS

The Introduction, Summary, and "Multiscaling in Biomolecular Modeling and Simulation" were written by T.S. and S. P.-L. "Electromechanical Multiscale Modeling of Cancelous Bone" was written by M.B. and K.H. " Stabilized and Variational Multiscale Methods for Multiphysics Problems" was written by A.M. "A Multiresolution Wavelet Method for Multiscale and Multiphysics Applications" was written by C.H., L.D., K.M., and D.L. "Parametrically Homogenized Constitutive Models for Multiscale Modeling of Deformation and Crack Nucleation in Titanium Alloys" was written by S.G. and S.K. "Multiscale Modeling for Dynamics of Architected Materials and Structures" was written by C.O. "Multiscaling for Reinforced Concrete Structures" was written by J.F. and A.M.

REFERENCES

Altair Multiscale Designer. Material Model Development Framework. https://www.altair.com/multiscale-designer/. Accessed: 2021-03-22.

American Concrete Institute Committee 318. Building Code Requirements for Structural Concrete, Technical Report, American Concrete Institute, 2014.

Anahid, M., Samal, M.K., and Ghosh, S., Dwell Fatigue Crack Nucleation Model Based on Crystal Plasticity Finite Element Simulations of Polycrystalline Titanium Alloys, *J. Mech. Phys. Solids*, vol. **59**, no. 10, pp. 2157–2176, 2011.

Arbogast, T., Implementation of a Locally Conservative Numerical Subgrid Upscaling Scheme for Two-Phase Darcy Flow, *Comput. Geosci.*, vol. **6**, nos. 3-4, pp. 453–481, 2002.

Bagri, A., Weber, G., Stinville, J.-C., Lenthe, W., Pollock, T., Woodward, C., and Ghosh, S., Microstructure and Property-Based Statistically Equivalent Representative Volume Elements for Polycrystalline Ni-Based Superalloys Containing Annealing Twins, *Metall. Mater. Trans. A*, vol. **49**, no. 11, pp. 5727–5744, 2018.

Bascom, G., Myers, C., and Schlick, T., Mesoscale Modeling Reveals Formation of an Epigenetically Driven HOXC Gene Hubs, *Proc. Natl. Acad. Sci. USA*, vol. **116**, no. 11, pp. 4955–4962, 2018.

Bascom, G. and Schlick, T., Linking Chromatin Fibers to Gene Folding by Hierarchical Looping, *Biophys. J.*, vol. **112**, no. 3, pp. 434–445, 2017.

Bazilevs, Y., Calo, V., Cottrell, J., Hughes, T., Reali, A., and Scovazzi, G., Variational Multiscale Residual-Based Turbulence Modeling for Large Eddy Simulation of Incompressible Flows, *Comput. Methods Appl. Mech. Eng.*, vol. **197**, no. 1, pp. 173–201, 2007.

Beard, D.A. and Schlick, T., Modeling Salt-Mediated Electrostatics of Macromolecules: The Discrete Surface Charge Optimization Algorithm and Its Application to the Nucleosome, *Biopolymers*, vol. **58**, no. 1, pp. 106–115, 2001.

Benek, J.A., Steger, J., Dougherty, F., and Buning, P., Chimera: A Grid-Embedding Technique, Technical Report, Arnold Engineering Development Center, United States Air Force, 1989.

Berger, M.J. and Oliger, J., Adaptive Mesh Refinement for Hyperbolic Partial Differential Equations, *J. Comput. Phys.*, vol. **53**, pp. 484–512, 1984.

Bertoluzza, S., Adaptive Wavelet Collocation Method for the Solution of Burgers Equation, *Transp. Theor. Stat.*, vol. **25**, pp. 339–352, 1996.

Beylkin, G. and Keiser, J.M., On the Adaptive Numerical Solution of Nonlinear Partial Differential Equations in Wavelet Bases, *J. Comput. Phys.*, vol. **132**, pp. 233–259, 1997.

Biswas, J.K., Roy, S., Pradhan, R., Rana, M., and Majumdar, S., Effects of Cervical Disc Replacement and Anterior Fusion for Different Bone Conditions: A Finite Element Study, *Int. J. Multiscale Comput. Eng.*, vol. **17**, no. 4, pp. 411–427, 2019.

Blaszczyk, M. and Hackl, K., A Fully Coupled Two-Phase Bone Material Model, *PAMM*, vol. **20**, no. 1, p. e202000144, 2021a.

Blaszczyk, M. and Hackl, K., Multiscale Modeling of Cancellous Bone Considering Full Coupling of Mechanical, Electrical and Magnetic Effects, arXiv:2106.06343, 2021b.

Boslough, M., Jennings, B., Carvey, B., and Fogleman, W., Fema Asteroid Impact Tabletop Exercise Simulations, *Procedia Eng.*, vol. **103**, pp. 43–51, 2015.

Brandt, A., Multi-Level Adaptive Solutions to Boundary-Value Problems, *Math. Comput.*, vol. **31**, p. 333, 1977.

Brezzi, F., Franca, L., Hughes, T., and Russo, A., b = infinite g, *Comput. Methods Appl. Mech. Eng.*, vol. **145**, no. 3, pp. 329–339, 1997.

Brezzi, F., Marini, D., and Russo, A., Applications of the Pseudo Residual-Free Bubbles to the Stabilization of Convection-Diffusion Problems, *Comput. Methods Appl. Mech. Eng.*, vol. **166**, no. 1, pp. 51–63, 1998.

Brooks, A.N. and Hughes, T.J., Streamline Upwind/Petrov–Galerkin Formulations for Convection Dominated Flows with Particular Emphasis on the Incompressible Navier–Stokes Equations, *Comput. Methods Appl. Mech. Eng.*, vol. **32**, no. 1, pp. 199–259, 1982.

Cai, X., Liang, J., Deiterding, R., Che, Y., and Lin, Z., Adaptive Mesh Refinement Based Simulations of Three-Dimensional Detonation Combustion in Supersonic Combustible Mixtures with a Detailed Reaction Model, *Int. J. Hydrog. Energy*, vol. **41**, pp. 3222–3239, 2016.

Calderer, R. and Masud, A., Residual-Based Variational Multiscale Turbulence Models for Unstructured Tetrahedral Meshes, *Comput. Methods Appl. Mech. Eng.*, vol. **254**, pp. 238–253, 2013.

Casadei, F., Rimoli, J.J., and Ruzzene, M., Multiscale Finite Element Analysis of Wave Propagation in Periodic Solids, *Finite Elem. Anal. Des.*, vol. **108**, pp. 81–95, 2016.

Castanier, M.P., Tan, Y.C., and Pierre, C., Characteristic Constraint Modes for Component Mode Synthesis, *AIAA J.*, vol. **39**, no. 6, pp. 1182–1187, 2001.

Chapelle, D., Tallec, P.L., Moireau, P., and Sorine, M., Energy-Preserving Muscle Tissue Model: Formulation and Compatible Discretizations, *Int. J. Multiscale Comput. Eng.*, vol. **10**, no. 2, pp. 189–211, 2012.

Chen, P., Wijaya, I.P., Tuttle, I., and Masud, A., Interfacial Coupling Across Incompatible Meshes in a Monolithic Finite-Strain thermomechanical Formulation, Comput. Math. Appl., vol. **79**, no. 11, pp. 3068–3091, 2020.

Codina, R., Principe, J., Guasch, O., and Badia, S., Time Dependent Subscales in the Stabilized Finite Element Approximation of Incompressible Flow Problems, *Comput. Methods Appl. Mech. Eng.*, vol. **196**, no. 21, pp. 2413–2430, 2007.

Collepardo-Guevara, R., Portella, G., Vendruscolo, M., Frenkel, D., Schlick, T., and Orozco, M., Chromatin Unfolding by Epigenetic Modifications Explained by Dramatic Impairment of Internucleosome Interactions: A Multiscale Computational Study, *J. Am. Chem. Soc.*, vol. **137**, no. 32, pp. 10205–10215, 2015.

Colomés, O., Badia, S., Codina, R., and Principe, J., Assessment of Variational Multiscale Models for the Large Eddy Simulation of Turbulent Incompressible Flows, *Comput. Methods Appl. Mech. Eng.*, vol. **285**, pp. 32–63, 2015.

Craig, R. and Bampton, M., Coupling of Substructures for Dynamic Analyses, *AIAA J.*, vol. **6**, no. 7, pp. 1313–1319, 1968.

Dubos, T. and Kevlahan, N.K., A Conservative Adaptive Wavelet Method for the Shallow-Water Equations on Staggered Grids, *Q. J. R. Meteorol. Soc.*, vol. **139**, pp. 1997–2020, 2013.

Eagen, K., Hartl, T., and Kornberg, R., Stable Chromosome Condensation Revealed by Chromosome Conformation Capture, *Cell*, vol. **163**, no. 4, pp. 934–946, 2015.

Fatkullin, I. and Hesthaven, J.S., Adaptive High-Order Finite-Difference Method for Nonlinear Wave Problems, *J. Sci. Comput.*, vol. **16**, pp. 47–67, 2001.

Fehlberg, E., Classical Fourth- and Lower Order Runge–Kutta Formulas with Stepsize Control and their Application to Heat Transfer Problems, *Computing*, vol. **6**, pp. 61–71, 1970.

Filonova, V., Fafalis, D., and Fish, J., Dispersive Computational Continua, *Comput. Methods Appl. Mech. Eng.*, vol. **298**, pp. 58–79, 2016.

Fish, J., Chen, W., and Nagai, G., Non-Local Dispersive Model for Wave Propagation in Heterogeneous Media: Multi-Dimensional Case, *Int. J. Numer. Methods Eng.*, vol. **54**, pp. 347–363 (2002a).

Fish, J., Chen, W., and Nagai, G., Non-Local Dispersive Model for Wave Propagation in Heterogeneous Media: One-Dimensional Case, *Int. J. Numer. Methods Eng.*, vol. **54**, no. 3, pp. 331–346 (2002b).

Fish, J., Wagner, G.J., and Keten, S., Mesoscopic and Multiscale Modelling in Materials., *Nat. Mater.*, vol. **20**, no. 6, pp. 774–786, 2021.

Franca, L.P., Hauke, G., and Masud, A., Revisiting Stabilized Finite Element Methods for the Advective–Diffusive Equation, *Comput. Methods Appl. Mech. Eng.*, vol. **195**, no. 13, pp. 1560–1572, 2006.

Fröhlich, J. and Schneider, K., An Adaptive Wavelet Galerkin Algorithm for One- and Two-Dimensional Frame Computations, *Eur. J. Mech.*, vol. **13**, pp. 439–471, 1994.

Fukada, E. and Yasuda, I., On the Piezoelectric Effect of Bone, *JPSJ*, vol. **12**, no. 10, pp. 1158–1162, 1957.

Gilbert, R.P., Fang, M., Guyenne, P., and Vasilic, A., Numerical Homogenization of the Timeharmonic Acoustics of Bone: The Monophasic Case, *Int. J. Multiscale Comput. Eng.*, vol. **5**, no. 6, pp. 461–471, 2007.

Goedecker, S. Wavelets and their Application for the Solution of Partial Differential Equations in Physics, Technical Report, Max-Planck Institute for Solid State Research, 1998.

Gómez-García, P.A., Portillo-Ledesma, S., Neguembor, M.V., Pesaresi, M., Oweis, W., Rohrlich, T., Wieser, S., Meshorer, E., Schlick, T., Cosma, M.P., and Lakadamyali, M., Mesoscale Modeling and Single-Nucleosome Tracking Reveal Remodeling of Clutch Folding and Dynamics in Stem Cell Differentiation, *Cell Rep.*, vol. **34**, no. 2, p. 108614, 2021.

Grigoryev, S.A., Bascom, G., Buckwalter, J.M., Schubert, M.B., Woodcock, C.L., and Schlick, T., Hierarchical Looping of Zigzag Nucleosome Chains in Metaphase Chromosomes, *Proc. Natl. Acad. Sci. USA*, vol. **113**, no. 5, pp. 1238–1243, 2016.

Gui, W. and Babuška, I., The h,p and h-p Versions of the Finite Element Method in 1 Dimension, Part I. The Error Analysis of the p-Version, *Numerische Mathematik*, vol. **49**, no. 6, pp. 577–612, 1986.

Güzelsu, N. and Saha, S., Electro-Mechanical Wave Propagation in Long Bones, *J. Biomech.*, vol. **14**, no. 1, pp. 19–33, 1981.

Hamed, E., Lee, Y., and Jasiuk, I., Multiscale Modeling of Elastic Properties of Cortical Bone, *Acta Mech.*, vol. **213**, no. 1, pp. 131–154, 2010.

Harnish, C., Matouš, K., and Livescu, D., Adaptive Wavelet Algorithm for Solving Nonlinear Initialboundary Value Problems with Error Control, *Int. J. Multiscale Comput. Eng.*, vol. **16**, no. 1, pp. 19–43, 2018.

Harnish, C., Dalessandro, L., Matouš, K., and Livescu, D., A Multiresolution Adaptive Wavelet Method for Nonlinear Partial Differential Equations, *Int. J. Multiscale Comput. Eng.*, vol. **19**, no. 2, pp. 29–37, 2021.

Hauke, G. and Garcia-Olivares, A., Variational Subgrid Scale Formulations for the Advection–Diffusion-Reaction Equation, *Comput. Methods Appl. Mech. Eng.*, vol. **190**, no. 51, pp. 6847–6865, 2001.

Hill, R., Elastic Properties of Reinforced Solids: Some Theoretical Principles, *J. Mech. Phys. Solids*, vol. **11**, no. 5, pp. 357–372, 1963.

Holmström, M., Solving Hyperbolic PDEs Using Interpolating Wavelets, *SIAM J. Sci. Comput.*, vol. **21**, no. 2, pp. 405–420, 1999.

Hu, R. and Oskay, C., Nonlocal Homogenization Model for Wave Dispersion and Attenuation in Elastic and Viscoelastic Periodic Layered Media, *J. Appl. Mech.*, vol. **84**, no. 3, p. 031003, 2017.

Hu, R. and Oskay, C., Spatial–Temporal Nonlocal Homogenization Model for Transient Anti-Plane Shear Wave Propagation in Periodic Viscoelastic Composites, *Comput. Meth. Appl. Mech. Eng.*, vol. **342**, pp. 1–31, 2018.

Hu, R. and Oskay, C., Multiscale Nonlocal Effective Medium Model for In-Plane Elastic Wave Dispersion and Attenuation in Periodic Composites, *J. Mech. Phys. Solids*, vol. **124**, pp. 220–243, 2019.

Hu, R. and Oskay, C., Spectral Variational Multiscale Model for Transient Dynamics of Phononic Crystals and Acoustic Metamaterials, *Comput. Meth. Appl. Mech. Eng.*, vol. **359**, p. 112761, 2020.

Huang, S., Yuan, Z., and Fish, J., Computational Framework for Short-Steel Fiber-Reinforced Ultrahigh Performance Concrete (COR-TUF), *Int. J. Multiscale Comput. Eng.*, vol. **17**, no. 5, pp. 551–562, 2019.

Hughes, T.J., Multiscale Phenomena: Green's Functions, the Dirichlet-to-Neumann Formulation, Subgrid Scale Models, Bubbles and the Origins of Stabilized Methods, *Comput. Methods Appl. Mech. Eng.*, vol. **127**, no. 1, pp. 387–401, 1995.

Hughes, T.J. and Franca, L.P., A New Finite Element Formulation for Computational Fluid Dynamics: VII. The Stokes Problem with Various Well-Posed Boundary Conditions, Symmetric Formulations that Converge for All Velocity/Pressure Spaces, *Comput. Methods Appl. Mech. Eng.*, vol. **65**, no. 1, pp. 85–96, 1987.

Hughes, T.J., Feijóo, G.R., Mazzei, L., and Quincy, J.-B., The Variational Multiscale Method—A Paradigm for Computational Mechanics, *Comput. Methods Appl. Mech. Eng.*, vol. **166**, nos. 1-2, pp. 3–24, 1998a.

Hughes, T.J.R., Feijóo, G.R., Mazzei, L., and Quincy, J.B., The Variational Multiscale Method—A Paradigm for Computational Mechanics, *Comput. Methods Appl. Mech. Eng.*, vol. **166**, no. 1-2, pp. 3–24, 1998b.

Hui, T. and Oskay, C., A Nonlocal Homogenization Model for Wave Dispersion in Dissipative Composite Materials, *Int. J. Solids Struct.*, vol. **50**, pp. 38–48, 2013.

Hui, T. and Oskay, C., A High Order Homogenization Model for Transient Dynamics of Heterogeneous Media Including Micro-Inertia Effects, *Comput. Methods Appl. Mech. Eng.*, vol. **273**, pp. 181–203, 2014.

Hui, T. and Oskay, C., Laplace-Domain, High-Order Homogenization for Transient Dynamic Response of Viscoelastic Composites, *Int. J. Numer. Meth. Eng.*, vol. **103**, pp. 937–957, 2015.

Ilic, S., Hackl, K., and Gilbert, R.P., Application of the Multiscale FEM to the Modeling of Cancellous Bone, *Biomech. Model. Mechan.*, vol. **9**, no. 1, pp. 87–102, 2010.

Iqbal, A. and Jeoti, V., An Improved Split-Step Wavelet Transform Method for Anomalous Radio Wave Propagation Modeling, *Radio Eng.*, vol. **23**, pp. 987–996, 2014.

Jawerth, B. and Sweldens, W., Overview of Wavelet Based Multiresolution Analyses, *SIAM Rev.*, vol. **36**, pp. 377–412, 1994.

Kaina, N., Lemoult, F., Fink, M., and Lerosey, G., Negative Refractive Index and Acoustic Superlens from Multiple Scattering in Single Negative Metamaterials, *Nature*, vol. **525**, pp. 77–81, 2015.

Kaufman, J.J., Luo, G., and Siffert, R.S., Ultrasound Simulation in Bone, *IEEE Trans Ultrason Ferroelec. Freq. Control*, vol. **55**, no. 6, p. 1205–1218, 2008.

Khelif, A., Choujaa, A., Benchabane, S., Djafari-Rouhani, B., and Laude, V., Guiding and Bending of Acoustic Waves in Highly Confined Phononic Crystal Waveguides, *Appl. Phys. Lett.*, vol. **84**, no. 22, pp. 4400–4402, 2004.

Kirchdoerfer, T. and Ortiz, M., Data-Driven Computational Mechanics, *Comput. Methods Appl. Mech. Eng.*, vol. **304**, no. 1, pp. 81–101, 2016.

Kong, F., Kougioumtzoglou, I.A., Spanos, P.D., and Li, S., Nonlinear System Response Evolutionary Power Spectral Density Determination via a Harmonic Wavelets Based Galerkin Technique, *Int. J. Multiscale Comput. Eng.*, vol. **14**, no. 3, pp. 255–272, 2016.

Kornberg, R.D., Structure of Chromatin, *Annu. Rev. Biochem.*, vol. **46**, no. 1, pp. 931–954, 1977.

Kotha, S., Ozturk, D., and Ghosh, S., Parametrically Homogenized Constitutive Models (PHCMs) from Micromechanical Crystal Plasticity Fe Simulations, Part I: Sensitivity Analysis and Parameter Identification for Titanium Alloys, *Int. J. Plast*, vol. **120**, pp. 296–319, 2019a.

Kotha, S., Ozturk, D., and Ghosh, S., Parametrically Homogenized Constitutive Models (PHCMs) from Micromechanical Crystal Plasticity Fe Simulations: Part II: Thermo-Elasto-Plastic Model with Experimental Validation for Titanium Alloys, *Int. J. Plast*, vol. **120**, pp. 320–339, 2019b.

Kotha, S., Ozturk, D., and Ghosh, S., Uncertainty-Quantified Parametrically Homogenized Constitutive Models (UQ-PHCMs) for Dual-Phase α/β Titanium Alloys, *npj Comput. Mater.*, vol. **6**, no. 1, p. 117, 2020a.

Kotha, S., Ozturk, D., Smarslok, B., and Ghosh, S., Uncertainty Quantified Parametrically Homogenized Constitutive Models for Microstructure-Integrated Structural Simulations, *Integr. Mater. Manuf. Innov.*, vol. **9**, no. 4, pp. 322–338, 2020b.

Laboratoires Servier (2019). Osteoporosis. https://commons.wikimedia.org/wiki/File:Osteoporosis_–_Smart-Servier.jpg. Accessed: 2021-07-14.

Le, T.H. and Caracoglia, L., Reduced-Order Wavelet–Galerkin Solution for the Coupled, Nonlinear Stochastic Response of Slender Buildings in Transient Winds, *J. Sound Vib.*, vol. **344**, pp. 179–208, 2015.

Liandrat, J. and Tchamitchian, P., Resolution of the 1D Regularized Burgers Equation Using a Spatial Wavelet Approximation. Technical Report, NASA, 1990.

Lieberman-Aiden, E., van Berkum, N.L., Williams, L., Imakaev, M., Ragoczy, T., Telling, A., Amit, I., Lajoie, B.R., Sabo, P.J., Dorschner, M.O., Sandstrom, R., Bernstein, B., Bender, M.A., Groudine, M., Gnirke, A., Stamatoyannopoulos, J., Mirny, L.A., Lander, E.S., and Dekker, J., Comprehensive Mapping of Long Range Interactions Reveals Folding Principles of the Human Genome, *Science*, vol. **326**, no. 5950, pp. 289–293, 2009.

Lin, E.B. and Zhou, X., Connection Coeffcients on an Interval and Wavelet Solutions of Burgers Equation, *J. Comput. Appl. Math.*, vol. **135**, no. 1, pp. 63–78, 2001.

Liu, C. and Reina, C., Dynamic Homogenization of Resonant Elastic Metamaterials with Space/Time Modulation, *Comput. Mech.*, vol. **64**, pp. 147–161, 2019.

Maeshima, K., Tamura, S., Hansen, J.C., and Itoh, Y., Fluid-Like Chromatin: Toward Understanding the Real Chromatin Organization Present in the Cell, *Curr. Opin. Cell Biol.*, vol. **64**, pp. 77–89, 2020.

Malone, C.M., Nonaka, A., Woosley, S.E., Almgren, A.S., Bell, J.B., Dong, S., and Zingale, M., The Deflagration Stage of Chandrasekhar Mass Models for Type IA Supernovae, I. Early Evolution, *Astrophys. J.*, vol. **782**, no. 1, 2014.

Maloth, T., Ozturk, D., Hommer, G.M., Pilchak, A.L., Stebner, A.P., and Ghosh, S., Multiscale Modeling of Cruciform Dwell Tests with the Uncertainty-Quantified Parametrically Homogenized Constitutive Model, *Acta Mater.*, vol. **200**, pp. 893–907, 2020.

Masud, A. and Calderer, R., A Variational Multiscale Stabilized Formulation for the Incompressible Navier–Stokes Equations, *Comput. Mech.*, vol. **44**, no. 2, pp. 145–160, 2009.

Masud, A. and Calderer, R., A Variational Multiscale Method for Incompressible Turbulent Flows: Bubble Functions and Fine Scale Fields, *Comput. Methods Appl. Mech. Eng.*, vol. **200**, no. 33, pp. 2577–2593, 2011.

Masud, A. and Calderer, R., Residual-Based Turbulence Models for Moving Boundary Flows: Hierarchical Application of Variational Multiscale Method and Three-Level Scale Separation, *Int. J. Numer. Methods Fluids*, vol. **73**, no. 3, pp. 284–305, 2013.

Masud, A. and Franca, L.P., A Hierarchical Multiscale Framework for Problems with Multiscale Source Terms, *Comput. Methods Appl. Mech. Eng.*, vol. **197**, no. 33, pp. 2692–2700, 2008.

Masud, A. and Hughes, T.J., A Stabilized Mixed Finite Element Method for Darcy Flow, *Comput. Methods Appl. Mech. Eng.*, vol. **191**, no. 39, pp. 4341–4370, 2002.

Masud, A. and Khurram, R., A Multiscale/Stabilized Finite Element Method for the Advection–Diffusion Equation, *Comput. Methods Appl. Mech. Eng.*, vol. **193**, no. 21, pp. 1997–2018, 2004.

Masud, A. and Scovazzi, G., A Heterogeneous Multiscale Modeling Framework for Hierarchical Systems of Partial Differential Equations, *Int. J. Numer. Methods Fluids*, vol. **65**, nos. 1-3, pp. 28–42, 2011.

Masud, A. and Truster, T.J., A Framework for Residual-Based Stabilization of Incompressible Finite Elasticity: Stabilized Formulations and $\bar{F}$ Methods for Linear Triangles and Tetrahedra, *Comput. Methods Appl. Mech. Eng.*, vol. **267**, no. 1, pp. 359–399, 2013.

Masud, A., Truster, T.J., and Bergman, L.A., A Unified Formulation for Interface Coupling and Frictional Contact Modeling with Embedded Error Estimation, *Int. J. Numer. Methods Fluids*, vol. **92**, no. 2, pp. 141–177, 2012.

Masud, A. and Zhu, L., Variationally Derived Closure Models for Large Eddy Simulation of Incompressible Turbulent Flows, *Int. J. Numer. Methods Fluids*, vol. **93**, no. 7, pp. 2089–2120, 2021.

Matouš, K., Geers, M.G., Kouznetsova, V.G., and Gillman, A., A Review of Predictive Nonlinear Theories for Multiscale Modeling of Heterogeneous Materials, *J. Comput. Phys.*, vol. **330**, pp. 192–220, 2017.

Meng, S. and Guzina, B.B., On the Dynamic Homogenization of Periodic Media: Willis' Approach Versus Two-Scale Paradigm, *Proc. R. Soc., Ser. A*, vol. **474**, no. 2213, p. 20170638, 2018.

Miehe, C., Schröder, J., and Schotte, J., Computational Homogenization Analysis in Finite Plasticity Simulation of Texture Development in Polycrystalline Materials, *Comput. Methods Appl. Mech. Eng.*, vol. **171**, no. 3, pp. 387–418, 1999.

Miller, S.A., Horvath, A., and Monteiro, P.J.M., Impacts of Booming Concrete Production on Water Resources Worldwide, *Nat. Sustain.*, vol. **1**, no. 1, pp. 69–76, 2018.

Mousavi, S.H., Khanikaev, A.B., and Wang, Z., Topologically Protected Elastic Waves in Phononic Metamaterials, *Nat. Commun.*, vol. **6**, p. 8682, 2015.

Moyeda, A. and Fish, J., Multiscale Analysis of Prestressed Concrete Structures, *Int. J. Multiscale Comput. Eng.*, vol. **16**, no. 3, pp. 285–301, 2018a.

Moyeda, A. and Fish, J., Towards Practical Multiscale Approach for Analysis of Reinforced Concrete Structures, *Comput. Mech.*, vol. **62**, no. 4, pp. 685–700, 2018b.

Moyeda, A. and Fish, J., Multiscale Analysis of Solid, Waffle, Ribbed and Hollowcore Reinforced Concrete Slabs, *Comput. Methods Appl. Mech. Eng.*, vol. **348**, pp. 139–156, 2019.

Nassar, H., He, Q.-C., and Auffray, N., A Generalized Theory of Elastodynamic Homogenization for Periodic Media, *Int. J. Solids Struct.*, vol. **84**, pp. 139–146, 2016.

Nejadmalayeri, A., Vezolainen, A., Brown-Dymkoski, E., and Vasilyev, O.V., Parallel Adaptive Wavelet Collocation Method for PDEs, *J. Comput. Phys.*, vol. **298**, pp. 237–253, 2015.

Ou, H.D., Phan, S., Deerinck, T.J., Thor, A., Ellisman, M.H., and O'Shea, C.C., ChromEMT: Visualizing 3D Chromatin Structure and Compaction in Interphase and Mitotic Cells, *Science*, vol. **357**, no. 6349, p. eaag0025, 2017.

Ozer, G., Luque, A., and Schlick, T., The Chromatin Fiber: Multiscale Problems and Approaches, *Curr. Opin. Struc. Biol.*, vol. **31**, pp. 124–139, 2015.

Ozturk, D., Kotha, S., and Ghosh, S., An Uncertainty Quantification Framework for Multiscale Parametrically Homogenized Constitutive Models (PHCMs) of Polycrystalline Ti Alloys, *J Mech. Phys. Solids*, vol. **148**, p. 104294, 2021.

Ozturk, D., Kotha, S., Pilchak, A.L., and Ghosh, S., Parametrically Homogenized Constitutive Models (PHCMs) for Multi-Scale Predictions of Fatigue Crack Nucleation in Titanium Alloys, *JOM*, vol. **71**, no. 8, pp. 2657–2670, 2019a.

Ozturk, D., Kotha, S., Pilchak, A.L., and Ghosh, S., Two-Way Multi-Scaling for Predicting Fatigue Crack Nucleation in Titanium Alloys Using Parametrically Homogenized Constitutive Models, *J Mech. Phys. Solids*, vol. **128**, pp. 181–207, 2019b.

Ozturk, D., Pilchak, A., and Ghosh, S., Experimentally Validated Dwell and Cyclic Fatigue Crack Nucleation Model for Alpha–Titanium Alloys, *Scrip. Mater.*, vol. **127**, pp. 15–18, 2017.

Pahr, D.H. and Zysset, P.K., Influence of Boundary Conditions on Computed Apparent Elastic Properties of Cancellous Bone, *Biomech. Model. Mechan.*, vol. **7**, no. 6, pp. 463–476, 2008.

Pajak, M. and Ponikiewski, T., Flexural Behavior of Self-Compacting Concrete Reinforced with Different Types of Steel Fibers, *Const. Build. Mater.*, vol. **47**, pp. 397–408, 2013.

Paolucci, S., Zikoski, Z.J., and Wirasaet, D., WAMR: An Adaptive Wavelet Method for the Simulation of Compressible Reacting Flow. Part I. Accuracy and Effciency of Algorithm, *J. Comput. Phys.*, vol. **272**, pp. 814–841, 2014.

Portillo-Ledesma, S. and Schlick, T., Bridging Chromatin Structure and Function over a Range of Experimental Spatial and Temporal Scales by Molecular Modeling, *WIREs Comput. Mol. Sci.*, vol. **10**, no. 2, p. wcms.1434, 2020.

Portillo-Ledesma, S., Tsao, L.H., Wagley, M., Lakadamyali, M., Cosma, M.P., and Schlick, T., Nucleosome Clutches are Regulated by Chromatin Internal Parameters, *J. Mol. Biol.*, vol. **433**, no. 6, p. 166701, 2021.

Qian, S. and Weiss, J., Wavelets and the Numerical Solution of Partial Differential Equations, *J. Comput. Phys.*, vol. **106**, no. 1, pp. 155–175, 1993.

Rajagopal, A. and Sivakumar, S.M., A Combined R-H Adaptive Strategy Based on Material Forces and Error Assessment for Plane Problems and Bimaterial Interfaces, *Comput. Mech.*, vol. **41**, pp. 49–72, 2007.

Rao, S.S.P., Huang, S.-C., Glenn St Hilaire, B., Engreitz, J.M., Perez, E.M., Kieffer-Kwon, K.-R., Sanborn, A.L., Johnstone, S.E., Bascom, G.D., Bochkov, I.D., Huang, X., Shamim, M.S., Shin, J., Turner, D., Ye, Z., Omer, A.D., Robinson, J.T., Schlick, T., Bernstein, B.E., Casellas, R., Lander, E.S., and Aiden, E.L., Cohesin Loss Eliminates All Loop Domains., *Cell*, vol. **171**, no. 2, pp. 305–320, 2017.

Ringler, T., Petersen, M., Higdon, R.L., Jacobsen, D., Jones, P.W., and Maltrud, M., A Multiresolution Approach to Global Ocean Modeling, *Ocean Modelling*, vol. **69**, pp. 211–232, 2013.

Roca, D., Lloberas-Valls, O., Cante, J., and Oliver, J., A Computational Multiscale Homogenization Framework Accounting for Inertial Effects: Application to Acoustic Metamaterials Modelling, *Comput. Methods Appl. Mech. Eng.*, vol. **330**, pp. 415–446, 2018.

Rowley, M.J. and Corces, V.G., Organizational Principles of 3D Genome Architecture, *Nat. Rev. Genet.*, vol. **19**, no. 12, pp. 789–800, 2018.

Sakurai, T., Yoshimatsu, K., Schneider, K., Farge, M., Morishita, K., and Ishihara, T., Coherent Structure Extraction in Turbulent Channel Flow Using Boundary Adapted Wavelets, *J. Turbul.*, vol. **18**, pp. 352–372, 2017.

Schlick, T. *Molecular Modeling and Simulation: An Interdisciplinary Guide*, 2nd Ed., New York: Springer-Verlag, 2010.

Schlick, T., The 2013 Nobel Prize in Chemistry Celebrates Computations in Chemistry and Biology, *SIAM News*, vol. **46**, no. 10, pp. 1–4, 2013.

Schlick, T. and Department of Energy (2010). Scientific Grand Challenges, Opportunities in Biology at the Extreme Scale of Computing. Technical Reptort, U.S. Department of Energy.

Schlick, T. and Portillo-Ledesma, S., Biomolecular Modeling Thrives in the Age of Technology, *Nat. Comput. Sci.*, vol. **1**, pp. 321–331, 2021.

Schlick, T., Portillo-Ledesma, S., Myers, C., Beljak, L., Chen, J., Dakhel, S., Darling, D., Ghosh, S., Hall, J., Jan, M., Liang, E., Saju, S., Vohr, M., Wu, C., Xu, Y., and Xue, E., Biomolecular Modeling and Simulation: A Prospering Multidisciplinary Field, *Annu. Rev. Biophys.*, vol. **50**, pp. 267–301, 2021a.

Schlick, T., Zhu, Q., Dey, A., Jain, S., Yan, S., and Laederach, A., To Knot or not to Knot: Multiple Conformations of the SARS-CoV-2 Frameshifting RNA Element, *J. Am. Chem. Soc.*, In press, 2021b.

Schlick, T., Zhu, Q., Jain, S., and Yan, S., Structure-Altering Mutations of the SARS-CoV-2 Frameshifting RNA Element, *Biophys. J.*, vol. **120**, no. 6, pp. 1040–1053, 2021c.

Schneider, K. and Vasilyev, O.V., Wavelet Methods in Computational Fluid Dynamics, *Annu. Rev. Fluid Mech.*, vol. **42**, pp. 473–503, 2010.

Schröder, J. and Hackl, K. *Plasticity and Beyond: Microstructures, Crystal-Plasticity and Phase Transitions*, CISM International Centre for Mechanical Sciences, Springer: Vienna, 2013.

Semenov, A.S., Kessler, H., Liskowsky, A., and Balke, H., On a Vector Potential Formulation for 3D Electromechanical Finite Element Analysis, *Commun. Numer. Methods Eng.*, vol. **22**, no. 5, pp. 357–375, 2006.

Speicher, M.R. and Carter, N.P., The New Cytogenetics: Blurring the Boundaries with Molecular Biology, *Nat. Rev. Genet.*, vol. **6**, no. 10, pp. 782–792, 2005.

Sridhar, A., Kouznetsova, V.G., and Geers, M.G.D., Homogenization of Locally Resonant Acoustic Metamaterials towards an Emergent Enriched Continuum, *Comput. Mech.*, vol. **57**, no. 3, pp. 423–435, 2016.

Sridhar, A., Kouznetsova, V.G., and Geers, M.G.D., A General Multiscale Framework for the Emergent Effective Elastodynamics of Metamaterials, *J. Mech. Phys. Solids*, vol. **111**, pp. 414–433, 2018.

Steeb, H., Ultrasound Propagation in Cancellous Bone, *Arch. Appl. Mech.*, vol. **80**, no. 5, pp. 489–502, 2010.

Stenger, N., Wilhelm, M., and Wegener, M., Experiments on Elastic Cloaking in thin Plates, *Phys. Rev. Lett.*, vol. **108**, no. 1, p. 014301, 2012.

Tal, D. and Fish, J., Stochastic Multiscale Modeling and Simulation Framework for Concrete, C*em. Concr. Compos.*, vol. **90**, pp. 61–81, 2018.

Trainor, K.J., Foust, B.W., and Landis, E.N., Measurement of Energy Dissipation Mechanisms in Fracture of Fiber-Reinforced Ultrahigh-Strength Cement-Based Composites, *J. Eng. Mech.*, vol. **139**, no. 7, pp. 771–779, 2013.

Truster, T.J. and Masud, A., Primal Interface Formulation for Coupling Multiple PDEs: A Consistent Derivation via the Variational Multiscale Method, *Comput. Methods Appl. Mech. Eng.*, vol. **268**, pp. 194–224, 2014.

Ueno, T., Ide, T., and Okada, M., A Wavelet Collocation Method for Evolution Equations with Energy Conservation Property, *Bull. Sci. Math.*, vol. **127**, no. 6, pp. 569–583, 2003.

Vallicotti, D., Sridhar, A., and Keip, M.-A., Variationally Consistent Computational Homogenization of Micro-Electro-Mechanics at Finite Deformations, *Int. J. Multiscale Comput. Eng.*, vol. **16**, no. 4, pp. 377–395, 2018.

van Tuijl, R.A., Harnish, C., Matouš, K., Remmers, J.J., and Geers, M.G., Wavelet Based Reduced Order Models for Microstructural Analyses, *Comput. Mech.*, vol. **63**, pp. 535–554, 2019.

Voigt, W., Ueber die Beziehung Zwischen den Beiden Elasticitätsconstanten Isotroper Körper, *Annalen der Physik*, vol. **274**, no. 12, pp. 573–587, 1889.

Wang, Y., Artz, T., Beel, A., Shao, X., and Fish, J., Computational Analyses of Flexural Behavior for Ultrahigh Performance Fiber Reinforced Concrete Bridge Decks, *Int. J. Multiscale Comput. Eng.*, vol. **18**, no. 4, pp. 477–491, 2020.

Yu, A., Pak, A.J., He, P., Monje-Galvan, V., Casalino, L., Gaieb, Z., Dommer, A.C., Amaro, R.E., and Voth, G.A., A Multiscale Coarse-Grained Model of the SARS-CoV-2 Virion, *Biophys. J.*, vol. **120**, no. 6, pp. 1097–1104, 2021.

Yushu, D. and Matouš, K., The Image-Based Multiscale Multigrid Solver, Preconditioner, and Reduced Order Model, *J. Comput. Phys.*, vol. **406**, p. 109165, 2020.

Yusufova, N., Kloetgen, A., Teater, M., Osunsade, A., Camarillo, J.M., Chin, C.R., Doane, A.S., Venters, B.J., Portillo-Ledesma, S., Conway, J., Phillip, J.M., Elemento, O., Scott, D.W., Béguelin, W., Licht, J.D., Kelleher, N.L., Staudt, L.M., Skoultchi, A.I., Keogh, M.-C., Apostolou, E., Mason, C.E., Imielinski, M., Schlick, T., David, Y., Tsirigos, A., Allis, C.D., Soshnev, A.A., Cesarman, E., and Melnick, A.M., Histone H1 Loss Drives Lymphoma by Disrupting 3D Chromatin Architecture, *Nature*, vol. **589**, no. 7841, pp. 299–305, 2021.

Zhu, L. and Masud, A., Variationally Derived Interface Stabilization for Discrete Multiphase Flows and Relation with the Ghost-Penalty Method, *Comput. Methods Appl. Mech. Eng.*, vol. **373**, p. 113404, 2021.